



This is the accepted version of this paper. The version of record is available at
<https://doi.org/10.1016/j.enconman.2022.115438>

Performance improvement of a desiccant based cooling system by mitigation of non-uniform illumination on the coupled Low Concentrating Photovoltaic Thermal units

Chandan^{a,b}, Hasan Baig^{d*}, Asif ali Tahir^d, K.S. Reddy^e, Tapas K. Mallick^d, Bala Pesala^{a,c}

^a Academy of Scientific and Innovative Research, Ghaziabad- 201002, India

^b CSIR-Structural Engineering Research Center, Chennai-600036, India

^c CSIR- Central Electronics Engineering Research Institute, Chennai-600113, India

^d Department of Mechanical Engineering, School of Engineering and the Environment, Roehampton Vale Campus, Kingston University, London, SW15 3DW, UK

^e Heat Transfer and Thermal Power Laboratory, Department of Mechanical Engineering, Indian Institute of Technology, Madras, Chennai 600 036, India

*H.Baig@kingston.ac.uk

Abstract

Low Concentrating photovoltaic thermal (LCPV/T) systems are finding application within process/refrigeration cycles to provide both electricity and low-grade thermal energy simultaneously while reducing the associated energy costs and carbon footprint. Typically, these Low Concentrating Photovoltaic Thermal systems employ Compound Parabolic Concentrators (CPC) or V-shaped mirrors to focus sunlight and enhance the quality of energy extracted. One of the major issues encountered whilst doing so is the introduction of non-uniform illumination on the PV panels which can reduce their electrical output thereby impacting the overall process efficiency. This non-uniform illumination can be mitigated by integrating homogenizers which are typically linear extensions to the Compound Parabolic Concentrators profile also referred to as Elongated Compound Parabolic Concentrators (ECPC). In this work, the performance of a 2.5x ECPC truncated to 1.7x and connected to a desiccant based cooling system has been explored. For a detailed analysis of the system, a coupled 3-D optical, electrical, thermal and process efficiency model has been developed. A full-scale prototype of the modelled system is also fabricated using a 380 W_p PV panel integrated into it. Experiments conducted on the developed system showed a peak outlet water temperature of 56°C at mass flowrate 24 LPH. Comparative studies between CPC and Elongated CPC based LCPV/T system is also presented to showcase the overall improvement in the process efficiency due to the mitigation of non-uniformity. Using a 400 mm length of the homogenizer the spatial non-uniformity factor dropped from 0.5 to 0.29 under normal incidence angle and results in a rise of 12% in the electrical output when compared to a CPC based system. The Coefficient of Performance (COP) of the desiccant-based air-cooling system is found to increase by 50% when coupled with two series-connected Elongated CPC based LCPV/T. The improvement in Coefficient of Performance is mainly because of thermal and electrical energy savings from the LCPV/T system amounting to 352 kWh_e/year and 665 kWh_{th}/year, respectively. Further, the mitigation of non-uniformity showed a performance improvement of 5% in the Coefficient of Performance of the air-cooling system compared to a Compound Parabolic Concentrators based system.

Keywords: Solar Energy, Co-generation, Compound Parabolic Concentrator, Non-Uniform Illumination, Concentrated Photovoltaic Thermal, desiccant based cooling

45 **Highlights**

- 46 • A comprehensive model to simulate desiccant based cooling system
 47 • Non-uniform illumination was found to reduce the electrical performance by 14%
 48 • Addition of homogenizer eliminates this loss completely and improves performance
 49 • Coupling the system with a desiccant based air cooler improved COP by 50%

50 **Nomenclature**

	Symbols	Units		Subscript
C_p	Specific heat at constant pressure	$J\ kg^{-1}\ ^\circ C^{-1}$	opt	Optical
C	Local concentration ratio	-	max	Maximum
CMH	Cubic meter per hour	$m^3\ h^{-1}$	min	Minimum
COP	Coefficient of performance	-	f	Fluid
D	Tube diameter	m	s	Solid
F	Potential function	-	el	Electrical
g	Acceleration due to gravity	$m\ s^{-2}$	abs	Absorber
G	Incident solar irradiance	$W\ m^{-2}$	o	Base
h_{conv}	Heat transfer coefficient	$W\ m^{-2}\ ^\circ C^{-1}$	conv	Convection
h	Enthalpy of air	$J\ kg^{-1}$	amb	Ambient
I	Current	A	L	Light
K_t	Boltzmann constant	-	S	Series
K	Thermal conductivity	$W\ m^{-1}\ K^{-1}$	Sh	Shunt
\dot{m}	Mass flow rate	$kg\ s^{-1}$	sen	Sensible
n	Diode factor	-	lat	Latent
N_s	No. of series-connected solar cells	-	ref	reference
P	Pressure	$N\ m^{-2}$	k	Variable
P_{ele}	Electrical power	W	comb	combined
Q	Thermal load	W	inc	incidence
\dot{q}	Heat flux	$W\ m^{-2}$	in	inlet
q_c	Charge of electron	$W\ m^{-3}$		Greek letters
q'_{gen}	Heat generated	$W\ m^{-3}$	α_{opt}	Spatial non-uniformity factor
R	Resistance	ohm	α	Thermal voltage (V)
r	rays	-	ρ	Density ($kg\ m^{-3}$)
Re	Reynolds no.	-	ρ_r	Reflectivity of the mirror
S	Flux	$W\ m^{-2}$	τ	Shear stress ($N\ m^{-2}$)
T	Temperature	K	η	Efficiency
u	Wind speed	$m\ s^{-1}$	β	Rate of degradation of the cells ($\% \ ^\circ C^{-1}$)
V	Voltage	V	ε	Effectiveness
V_f	Fluid velocity	$m\ s^{-1}$	ε_{sc}	Band gap of the solar cell
x	Concentration ratio		θ_a	Half acceptance angle
			μ_{sc}	Rate of degradation of the cells due to current ($\% \ ^\circ C^{-1}$)
			μ	Dynamic viscosity

51 1 Introduction

52 The impacts of climate change are increasingly being evidenced globally through surging daytime
53 temperatures and unexpected weather patterns. Major parts of tropical countries like India which
54 previously had an average comfortable daytime temperature and required no air-conditioning are
55 currently experiencing hotter day temperatures with peaks crossing 50°C. The average temperature in
56 India [1] has increased by 0.7°C during the last century and is expected to rise by approximately 4.4°C
57 by the end of 2100. Given the unbearable climate, people are bound to make excessive use of
58 refrigeration and air-conditioning processes to provide comfortable indoor living conditions. These
59 processes are highly energy-intensive and not yet cost-effective.

60 The dropping prices of solar photovoltaic (PV) technology, to some extent, has motivated people to
61 implement them within their households, still, a huge gap between consumption and generation
62 capacities exists [2]. The high Capex involved and singular benefit of electricity from PV modules limits
63 their application. With scorching day time temperatures, air conditioners (which already account for up
64 to 60-70% of the total energy load [3] in a typical building are being used more extensively than they
65 were a decade earlier. The ongoing pandemic has meant more people staying indoors and a surge in
66 power demand from hospitals, essential services, and the residential sector particularly for cooling
67 applications.

68 With an increasing impetus to deploy clean energy solutions, options are now being continuously
69 explored to combine PV technology within different applications to gain wider benefits. These could be
70 in the form of utilizing the excess heat rejected from the PV module after converting the solar radiation
71 to electricity. One such technology that effectively utilizes solar radiation is photovoltaic thermal (PV/T)
72 [4] systems. In PV/T systems, the PV panel generates electricity whereas the heat extraction unit/ heat
73 exchanger serves the dual purpose of cooling the PV panel and extracting the waste heat
74 simultaneously [5]. The use of solar-assisted air-conditioning cycles with PV/T is being explored as a
75 means to improve process efficiency. The biggest challenge with the existing PV/T system is the
76 generation of low-grade thermal output i.e. below 50°C [6] making it unsuitable for the regeneration of
77 the desiccant wheel, therefore limiting its application. This can however be overcome by concentrating
78 light onto the PV units [7]. When the solar concentration is less than 10x the systems are termed as
79 Low Concentrating Photovoltaic thermal (LCPV/T) [8] systems.

80 An LCPV/T system overcomes the limitation of a lower grade of thermal output from the PV/T systems
81 and can prove to be an effective mechanism of not only improving the process efficiency but also
82 lowering the overall cost. By providing electricity and thermal energy simultaneously these systems
83 reduce the requirements of rooftop areas per unit of energy being harnessed. Since these systems
84 generate both hot water and electricity, they can potentially be used for running thermally driven
85 cooling system.

86 Recently, a lot of work on thermally driven cooling system have been explored which includes vapor
87 absorption refrigeration system and desiccant based cooling system. Out of these two available
88 technologies, air-conditioning systems combined with rotary dehumidification is one of the popular
89 processes being currently deployed [9]. Recently, Liu et al. [10] numerically studied the performance of
90 a rotary desiccant wheel based air conditioner coupled to a solar thermal and a solar PV system to
91 match the electrical and thermal load of the system. Results showed that, with the increase in
92 regeneration temperature, an improvement in dehumidification and cooling capacity is observed. Tian
93 et al. [11] proposed a novel hybrid desiccant based air conditioner system integrated with a solar panel
94 and a multi evaporator and a multi condenser heat pump for a Near Zero Energy Building. Simulation
95 results show that the COP of the system was 3.4 in the summer months. Further, the results also
96 demonstrated that the daily energy consumption was 9% lower for temperature control mode and 12%

97 lower for humidity control mode. Wang et al.[12] explored the coupling of the PV/T system to a desiccant
98 based air conditioner. The thermal energy obtained from the PV/T system was stored in a PCM material
99 whereas the moisture laden return air from the desiccant wheel was used for the freshwater
100 production. Results show that at a mass flow rate of 0.31 kg/s of air, the COP of the combined system
101 was observed to be 0.41 with freshwater production of 4.91 L/h. Harrouz et al.[13] compared the
102 performance of conventional direct evaporative cooler and dew point indirect evaporative cooler coupled
103 with packed bed desiccant dehumidifier. Results show that dew point indirect evaporative cooler
104 required 35% lower operating cost compared to direct evaporative cooler. Low et al designed a liquid
105 desiccant-based air cooler coupled with a solar thermal collector and thermal energy storage system.
106 The reported overall system efficiency was observed to be 78.8%. Hu et al. [14] coupled a absorption
107 chiller with desiccant based dehumidifier system. Results showed such systems can improve the exergy
108 efficiency by 6-14% compared to conventional system. Zhou et al. [15] introduces an internally cooled
109 desiccant wheel for the cooling application of the building. Results show ~50% reduction in electrical
110 energy consumption compared to a conventional system. The work also demonstrated how low
111 temperature heat (~70°C) extracted from solar thermal collector can regenerate a desiccant wheel.
112 Jagirdar et al.[16] also demonstrated an internally cooled and heated desiccant heat coated exchanger.
113 The COP of the designed system was observed to be 9.8 whereas the effectiveness was observed to
114 be 0.88. In the present study, an effort has been made to model the performance of an air cooling
115 system with an integrated desiccant wheel-based air handling unit . In such thermally driven cooling
116 systems, the reduction in energy consumption is ~30-50% as reported by many literatures [17].

117 The present work focuses on the integration of the LCPV/T system to a desiccant based air cooler so a
118 brief review of the LCPV/T system is also presented below. For concentrating light onto the solar cells,
119 Compound Parabolic Concentrators (CPC) [18], V-trough [19], parabolic reflector [20], Fresnel reflector
120 [21], cross-compound parabolic concentrator [22], and so on have been explored in the past. CPC and
121 V-Trough concentrators are usually deployed for low concentration (1.1-2.5 \times) [23] systems where the
122 solar cells (monocrystalline silicon solar cells) operate at a lower temperature (60-80°C). Further, from
123 the literature, it is observed that CPC's are best suited for the LCPV/T systems because of its highest
124 average concentration ratio for the given acceptance angle [24]. Moreover, CPC's can effectively
125 concentrate direct and part of diffuse radiation [25] also making it an obvious choice for the
126 concentrators.

127 Previously, Haiping et al. [26] worked on a CPC-based LCPV/T system with a microchannels heat pipe
128 array. The heat pipe arrays were used to extract the waste heat from the PV panels. The reported
129 thermal and electrical efficiency was 54% and 14.4% respectively, at 60-70 litres per hour (LPH). The
130 experiments were conducted on the system for constant mass flowrate and constant outlet water
131 temperature. Li et al. [27] demonstrated a novel air gap lens walled CPC (ALCPC). The outlet water
132 temperature from the system was observed to be 70°C with a thermal and electrical efficiency of 35%
133 and 6% respectively. Hadavinia et al.[28] studied the electrical performance of CPC and V-trough at the
134 lab scale. The results proved that CPC gave 2.4% more power compared to V-Trough. Jazz et al. [29]
135 reported CPC based LCPV/T system with jet impingement cooling. Results show a 31% improvement
136 in power output from the PV module. Baig et al. [30] explored a 3-D Cross Compound Parabolic
137 Concentrator (CCPC). The effect of non-uniformity in flux distribution on the PV cell was studied. Results
138 showed that non-uniformity in the distribution of flux tends to reduce the short circuit current by 2.2%.
139 Chen et al. [31] explored asymmetric CPC for BIPV application. Baig et al. [32] reported a V-Trough
140 collector for the LCPV/T application. The rise in water temperature of 5.2°C was measured with the
141 water as a working fluid. Sharma et al. [33] worked on building an integrated CPV/T system integrated
142 with latent heat thermal storage material. The reduction in the operating temperature of solar cells due
143 to phase change material (PCM) material was observed, resulting in an improvement of efficiency by
144 7.7%. Heng et al. [34] compared the performance of the CPC based LCPV/T system with that of a PV/T

145 system. The experiment conducted on PV/T and LCPV/T showed that, by integrating a concentrator,
146 the thermal performance improves by two times and electrical power output improves three times.
147 Yousuf et al. [35] compared the performance of PV, PV/T, and LCPV/T system. It was observed that by
148 deploying a heat exchanger below the solar cells, an improvement in electrical efficiency by 11% in the
149 case of PV/T and 15% in the case of the LCPV/T system can be achieved. Widyolar et al. [36] studied
150 the performance of a non-imaging optics-based PV/T collector having aluminum mini channels for heat
151 removal. Results showed thermal and electrical efficiency of 57.4% and 12.3% respectively. Zhang et
152 al. [37] worked on HEMAR and LEMAR concentrators for LCPV/T applications. Thermal efficiency of
153 59% and electrical efficiency of 10.9% was reported. Raine et al.[38] explored geometrically optimized
154 circular rotational hyperboloid static concentrator for CPVT application. Results showed that 3x
155 concentrator had acceptance angle of $\pm 40^\circ$ with material requirement of 43% less compared to CCPC
156 of similar configuration. Xuan et al.[39] explored asymmetric dielectric-filled CPC for BIPV application.
157 Results show 96.6% improvement in power compared to a non-concentrating system with acceptance
158 angle of 0-85°. Li et al.[40] used exhaustive algorithm to generate a multi-sectioned CPC for LCPVT
159 application. Results showed 47% improvement in acceptance angle compared to a standard CPC.
160 Hatim et al.[41] developed a coupled optical and electrical analytical model for the PV-Thermo electric
161 system. Recently, Chandan et al. [42] studied the performance of a lab-scale CPC (10 cm x 10 cm
162 absorber) based LCPV/T system by integrating a homogenizer into it. Experimental results showed that
163 the integration of homogenizer improves the electrical efficiency by 23% compared to CPC of the same
164 geometrical concentration ratio. From the literature survey, it is observed that extensive work has been
165 carried out in the field of the CPC based LCPV/T system. However, there are very few pieces of literature
166 that have studied the causes and effects of non-uniform illumination on the electrical and thermal
167 performance of such an LCPV/T system [38].

168 In contrast to previous studies, the work presented here aims to expand the current literature on the
169 LCPV/T system by carrying out a detailed study on the optical, electrical, and thermal performance of
170 LCPV/T systems with and without the homogenizer for a system that has never been reported before.
171 It also attempts to showcase the study of the integration of the LCPV/T system to a desiccant based
172 cooling system. The new contribution of this paper can be summarized as follows:

- 173 • A detailed study on how the spatial-non-uniformity impacts the electrical performance of an
174 LCPV/T system and simple methods to reduce this impact
- 175 • Development of a novel coupled 3-D optical-electrical and thermal numerical modelling of a full-
176 scale CPC integrated with a homogenizer based LCPV/T
- 177 • Experimental validation of the numerical model is also carried out
- 178 • Comparative study of the thermal and electrical performance of a CPC based LCPV/T system
179 with and without a homogenizer is studied in detail
- 180 • Estimation of overall improvement in the performance of the desiccant-based air cooler when
181 coupled with such LCPV/T systems
- 182 • The benefits and drawbacks of using a homogenizer are highlighted and quantified
- 183 • A thorough study on the cost-benefit of implementing such a system is also presented

184 2 System Description

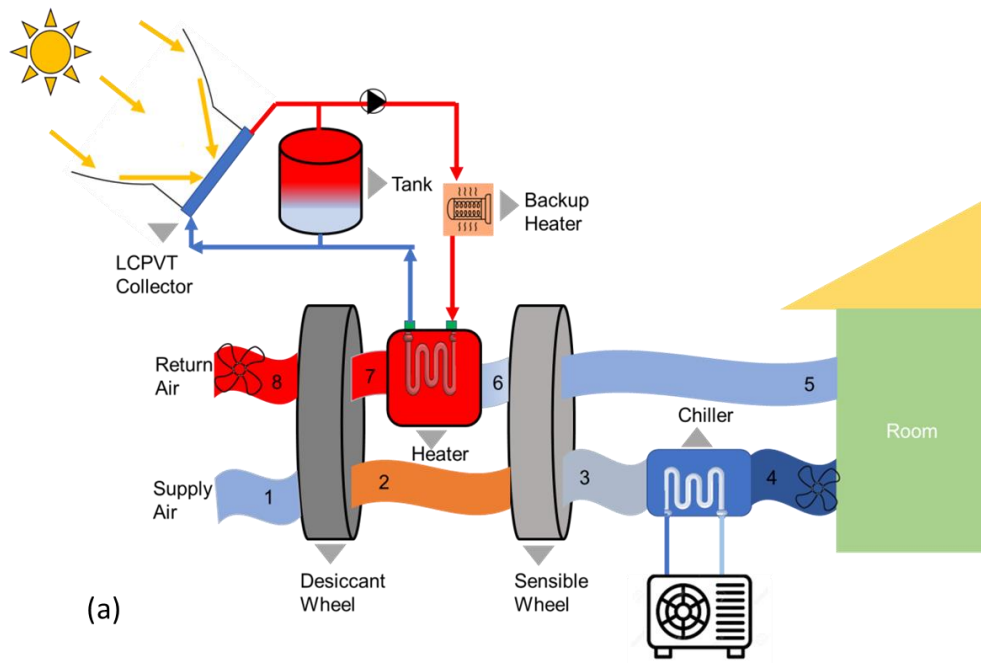
185 The combined system of the LCPV/T system and desiccant wheel-base air conditioning system can be
186 broadly classified into two heads i.e., heating subsystem and cooling subsystem. The heating
187 subsystem is made up of the LCPV/T system which can generate both thermal and electrical energy
188 simultaneously to regenerate the desiccant material and run the electrical components, respectively.
189 The cooling subsystem is made up of a desiccant based air conditioning system which reduces the

190 latent heat load of the air cooler and provides the cooling effect to the room. The subcomponents of
191 both systems are discussed in detail below.

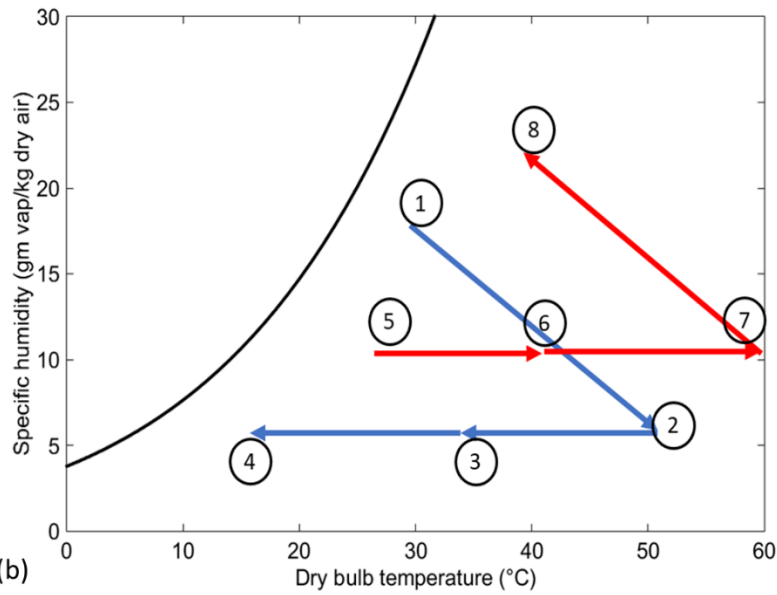
192 2.1 Components of desiccant based air-cooling system

193 The major components of the desiccant based air cooling system are a desiccant wheel, a heat recovery
194 wheel, a cooling coil, and a heating coil as shown in Figure 1(a) The desiccant wheel helps in the
195 adsorption of the moisture onto its surface. In the present case, the desiccant wheel is assumed to be
196 made up of silica gel. After the moisture is adsorbed to the surface of the desiccant material, the air gets
197 heated up. To cool the air sensibly, a heat recovery wheel/sensible wheel is used. The heat recovery
198 wheel is usually made up of an aluminum metal matrix due to its high thermal diffusibility. The air after
199 passing through the heat recovery wheel (having effectiveness 0.7) needs to be further conditioned to
200 bring it down to the comfortable condition of the room. This is achieved by passing the air through a
201 cooling coil. In the present case, the cooling coil is a portion of the evaporator of a vapour compression
202 refrigeration system (COP-4) exposed to process airflow. The cold air when enters the room, gains heat
203 from different thermal loads in the room such as heat gain through solar radiation, fenestration,
204 occupants in the room, electrical components in the room, and so on. In the present study, the room is
205 assumed to be of a size 49 m³. Further, the thermal load of the room is assumed to be fixed having a
206 sensible heat load of 1.37 kW and a latent heat load of 0.39 kW. Thereafter, the condition inside the
207 room is also fixed at 25°C and 60% RH with a mass flow rate of air on the supply side and return side
208 assumed to be 400 m³ hr⁻¹ each. A heating coil is also required to regenerate the desiccant wheel. In
209 this case, a heating coil is made up of thermal output from the LCPV/T system. It is further assumed
210 that, if the LCPV/T system is not able to achieve the regeneration temperature, then the external
211 electrical heater will be used to meet the thermal requirement for the regeneration of the air. Details
212 about the various processes are shown in table 1 where as details about other pieces of equipment are
213 listed in Table 2.

214



(a)



(b)

215

216

217

218

219

Figure 1(a) Schematic of the desiccant based cooling system (b) Process flow diagram of the desiccant based air cooling system

Table 1 Processes undergone by the air

Process	Effect	Components
1-2	Heating and dehumidification	Desiccant wheel (DW)
2-3	Sensible cooling	Sensible wheel (SW)
3-4	Additional Cooling	Cooling coil
4-5	Heating of air due to the thermal load of the building	Cooling space
5-6	Sensible heating of the air	Sensible wheel (SW)
6-7	Air heated to regeneration temperature of the desiccant wheel	Heating coil

220

221

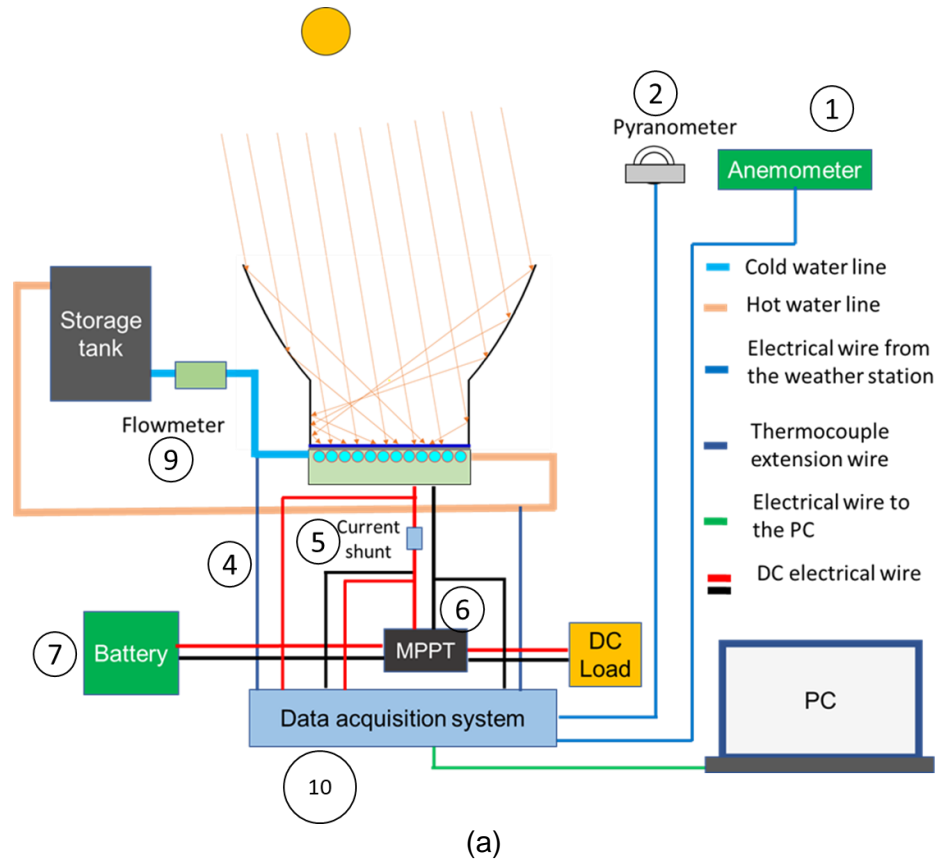
Table 2 specification of the desiccant wheel-based air cooler

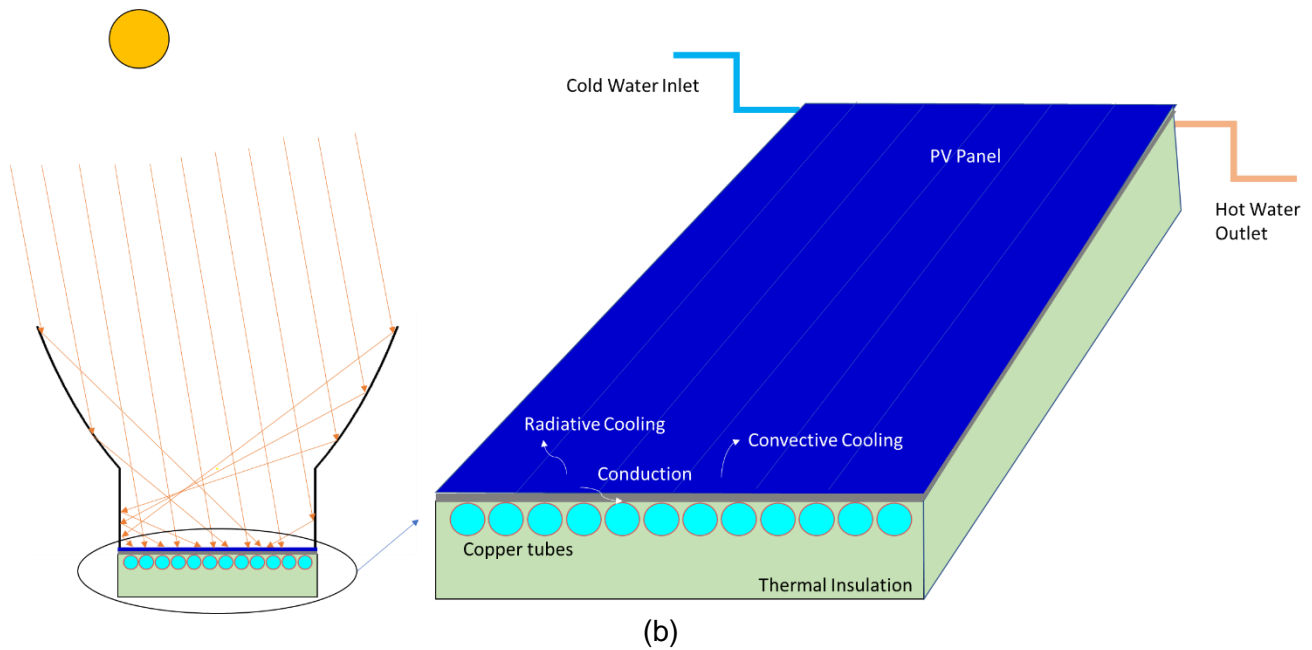
Component	Parameter
Axial blower	400 CMH x 2
Desiccant wheel	800 CMH
Sensible wheel	800 CMH
2 LCPV/T collector (series connected)	6.8 m ²

222

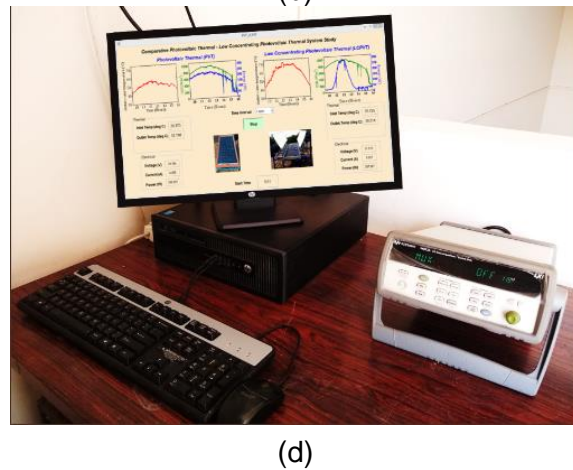
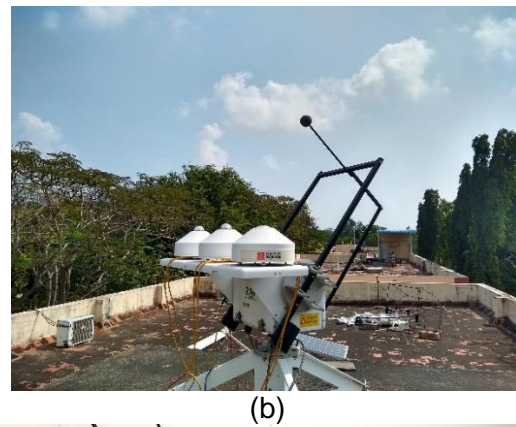
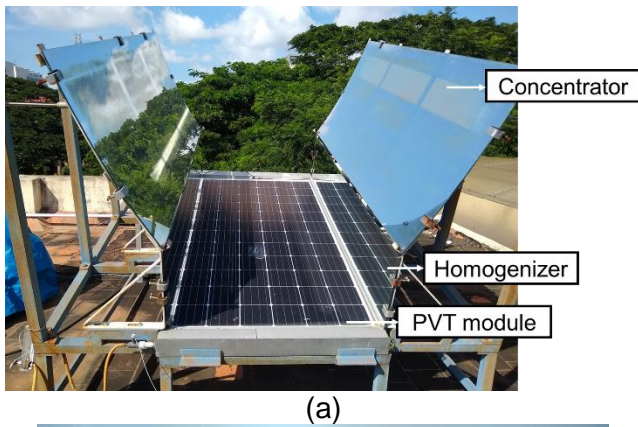
2.2 Experimental system setup

223 The LCPV/T system consists of a PV/T module integrated with a Compound Parabolic Concentrator
 224 and homogenizer. The non-Tracking LCPV/T system is placed in the N-S direction with a south-facing
 225 PV panel inclined at 13° as the latitude of Chennai is given as 13°N. The subcomponents of the LCPV/T
 226 systems are discussed in the section below. The schematic of the LCPV/T system, the pumping system
 227 and its associated testing equipment are shown in Figure 2(a). The mechanisms of heat transfer and
 228 the ray trace diagram are shown in Figure 2(b). Similarly, the overall experimental setup showcasing
 229 the PV/T with the homogenizer, the weather monitoring stations, and the data acquisition systems are
 230 shown in Figure 3.
 231





232 Figure 2 (a) Schematic of an LCPV/T system (b) Flux distribution due to the addition of homogenizer
 233 with CPC and the various heat transfer mechanisms occurring on the PV/T system
 234



235 Figure 3 (a) Fabricated LCPV/T system (b) Kipp and Zonen 2AP sun tracker for solar radiation
 236 measurement (c) Watch Dog Weather Station (d) Data Acquisition System.

237 **2.2.1 Photovoltaic thermal module**

238 A PV/T module consists of a PV panel, a heat exchanger, and an insulating material (glass wool) to
 239 prevent heat leakage from the back portion of the heat exchanger. The PV panel is a composite layer
 240 of PV glass, EVA sheet, PV cells, and Tedlar. The top glass gives rigidity to the PV panel while Tedlar
 241 prevents seepage of moisture into the cells. In general, a 380 W solar panel (dimension 1m x 2 m) has
 242 all the solar cells connected in series to generate the required voltage and current. The specification of
 243 the PV panel used in the setup is given in Table 3.

244 **Table-3 Specification of the PV panel**

PV Panel specification	PV panel
Dimension	1 m x 2 m
Open circuit voltage V_{oc}	47.74 V
Short Circuit Current I_{sc}	9.69 A
Maximum current	9.18 A
Maximum voltage	40.96 V
Maximum Power	380 W
Series resistance	

245

246 The PV panels when operating in the field; get heated up due to various reasons such as thermalization
 247 loss, bandgap loss, and recombination losses. The losses in the PV panel results in a higher operating
 248 temperature and reduced electrical efficiency. This high operating temperature of the PV panel can be
 249 brought down to a permissible limit by attaching a heat exchanger to the backside of the PV panel. The
 250 heat exchanger extracts the excess waste heat generated by the solar cells through a cooling medium
 251 such as cold water from the bottom direction of the PV panel. For the present case, the heat exchanger
 252 is made up of an aluminum sheet (1 m x 2 m x 0.004 m dimension). Twelve copper tubes of 16 mm
 253 outer dia. and 15 mm inner dia. are embedded in the bottom face of the aluminum sheet with the help
 254 of clamps. The gap between the tube and the sheet is filled with thermally conductive bonding material
 255 purchased from Dow (SE 4420 RTV sealant) having a thermal conductivity of $0.92 \text{ W m}^{-1} \text{ K}^{-1}$. The cold
 256 fluid is circulated inside the copper tube, and heat transfer takes place from the PV Panel to the cold
 257 circulating water, aluminum sheet and copper tube. The material properties of the heat exchanger are
 258 given in Table 4.

259 **Table – 4 Properties of the heat exchanger material**

Material	Dimension	Density (ρ) (kg m^{-3})	Specific heat capacity (C_p) ($\text{J kg}^{-1} \text{ }^\circ\text{C}^{-1}$)	Thermal conductivity (K) ($\text{W m}^{-2} \text{ }^\circ\text{C}^{-1}$)
Aluminum sheet	1 m x 2 m x 0.004 m	2700	900	280
Copper tube	16 mm o.d. and 15 mm i.d.	8700	385	400

260

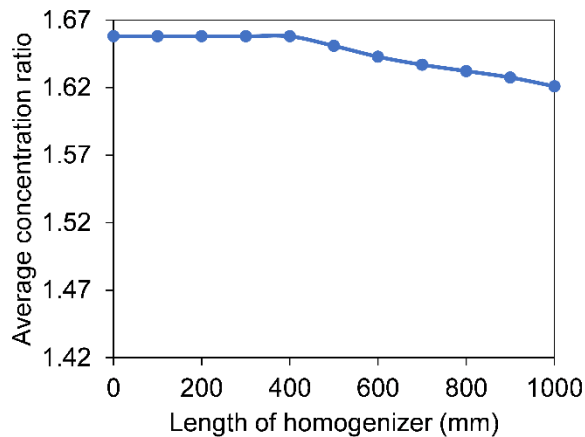
261 Concentrators are used to focus more solar radiation onto the PV/T module. For this work, a full CPC
 262 of geometrical concentration ratio of $2.5\times$ is truncated to $1.7\times$ has been explored. Initially, a CPC of $2\times$,
 263 $2.5\times$ and $3\times$ each truncated to $1.7\times$ was explored for the optical simulation. Results showed that $2\times$
 264 CPC had a higher acceptance angle (30°) however, the material required for the concentrator was also
 265 higher resulting in higher system cost. Thereafter, a CPC of concentration ratio of $3\times$ was also explored.
 266 With the increase in concentration ratio, a decrease in material requirement was observed with a
 267 reduced acceptance angle which resulted in lower operating hours. To overcome that, a CPC of $2.5\times$
 268 concentration ratio truncated to $1.7\times$ was explored. Which has a relatively higher acceptance angle and

269 lower material requirement thus making it cost-effective. The key reason for the truncation of the CPC
 270 to 1.7× was explored because previous experiments conducted at a high concentration ratio (2.5×)
 271 damaged both solar cells and concentrators in outdoor conditions.

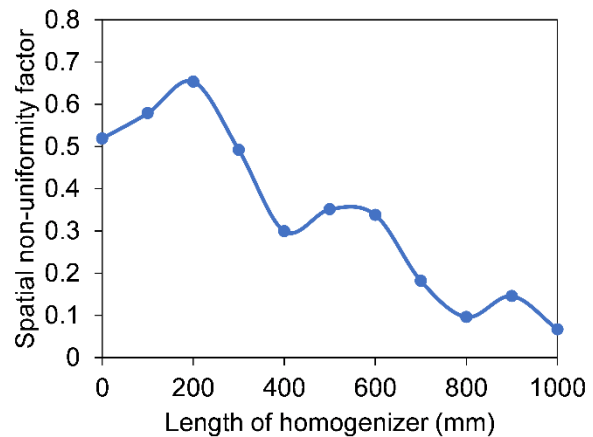
272 The CPC has a non-uniform distribution of flux. The non-uniform distribution of flux can be mitigated by
 273 integrating an optimized homogenizer. The homogenizers have been optimized by maximizing the
 274 average concentration ratio and reducing the spatial non-uniformity (α_{opt}) given by equation 1 [45]
 275 where C is the local concentration ratio.

$$\alpha_{opt} = \frac{C_{max} - C_{min}}{C_{max} + C_{min}} \quad (1)$$

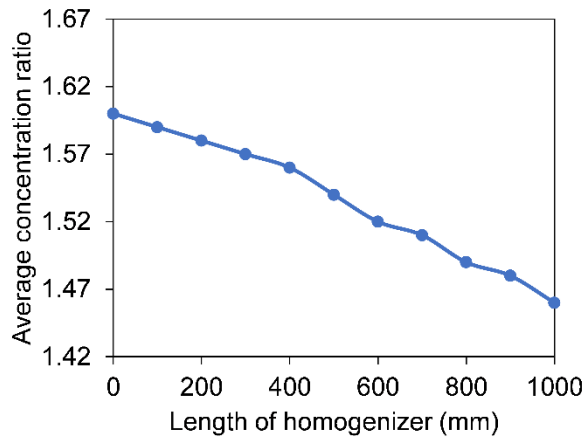
276 Optimization of the homogenizer is carried out by integrating a long homogenizer of length 1000 mm to
 277 the CPC. Thereafter, optical simulation is carried out on the CPC such that the length of the
 278 homogenizer is increased in the step of 100 mm until 1000 mm is reached. At each step of the
 279 homogenizer, the average optical concentration ratio falling on the absorber and spatial non-uniformity
 280 caused due to the integration of the concentrator are calculated as shown in Figure 4(a, b). From the
 281 optical simulations, it is observed that the 400 mm length of the homogenizer is optimal to reduce the
 282 non-uniform distribution of flux on the absorber area. For the homogenizer length of 400 mm, the spatial
 283 non-uniformity and the average concentration ratio are observed to be 0.29 and 1.66 respectively.
 284 Beyond 400 mm, the spatial non-uniformity factor reduces significantly resulting in a more uniform
 285 distribution of flux on the absorber area. Although the flux distribution is uniform, the multiple reflections
 286 from the homogenizer reduce the average concentration which is undesirable. Figure 4(c, d) shows the
 287 variation of average flux distribution and spatial non-uniformity on the PV/T panel when rays are falling
 288 on the CPC at a zenith angle of 10°.



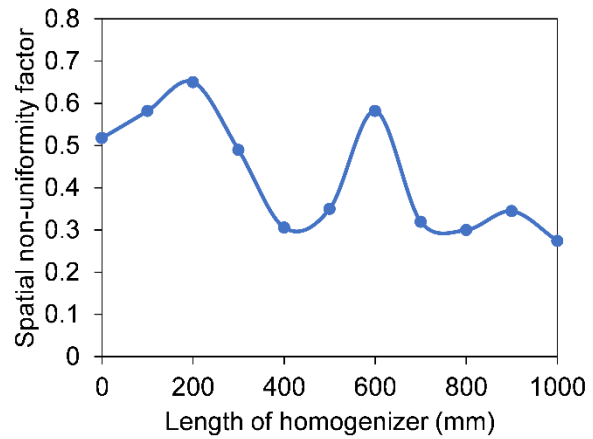
(a)



(b)



(c)



(d)

289 Figure 4 (a) Variation of average concentration ratio with the length of the homogenizer at a zenith angle
 290 of 0° (b) variation of spatial non-uniformity factor with the length of the homogenizer at zenith angle of
 291 0° (c) variation of average concentration ratio with the length of the homogenizer at zenith angle of
 292 10°(d) variation of spatial non-uniformity factor with the length of the homogenizer at a zenith angle of
 293 10°

294 It can be observed that, when rays enter the CPC at an angle, part of the rays are reflected out and thus
 295 they do not hit the absorber area because of which a lower average concentration ratio is observed.
 296 Based on the optical simulation, the profile of the concentrators is fabricated by a glass bending process
 297 in which the glass is bent into the shape of a CPC. The backside of the glass is coated with a reflective
 298 surface of reflectivity ~ 95%. The mirrors are then mounted on a mild steel structure for their application
 299 in the LCPV/T system. Table 5 shows the dimensions and properties of the concentrator.

300

Table 5 properties and dimensions of the concentrator

Parameter	Value
The reflectivity of the mirror (ρ_r)	0.95
Length of CPC mirror	2.00 m
Height of CPC mirror	0.74 m
Height of homogenizer	0.40 m
Geometrical concentration ratio (\times)	1.70
Effective half acceptance angle (θ_a)	22.57°

301

302 In the current case, the homogenizer is optimized for a 0° zenith angle. This length of the homogenizer
 303 has its limitation which will be discussed in the coming sections. It is proposed that, in the future study,
 304 the homogenizer will be optimized based on the angular study also.

305 2.2.2 Assembled Low Concentrating Photovoltaic Thermal system

306 The LCPV/T system has other auxiliary components such as water storage tanks (500L capacity) to
 307 store water, a pump (18W) to circulate cold water from the cold-water storage tank to the hot water
 308 storage tank through the heat exchanger, maximum power point tracker (MPPT) supplied by Phocos
 309 (Eco MPPT) to operate the PV panel at the maximum power point, battery (200 Ah capacity) to store
 310 extra electrical energy, and so on. Figure 3(a) shows the schematic of the assembled LCPV/T, whereas
 311 Figure 4(a) shows the actual system installed at CSIR CEERI Chennai.

312 For assessing the performance of the LCPV/T systems, various parameters such as temperature,
 313 voltage, current, irradiance, wind speed, wind direction, and ambient temperature need to be
 314 continuously monitored. For this purpose, the accurate measurement of these parameters become very
 315 important. To measure the temperature, calibrated K- Type thermocouples are used at the inlet and
 316 outlet of the heat exchanger. For measuring the electrical output from the PV panel, current and voltage
 317 are measured. Voltage is measured directly by connecting two wires across the two leads of the PV
 318 panel while current is measured indirectly with the help of a current shunt (75 mV, 10 A). The sampling
 319 time is set to 1 minute. The meteorological data such as direct and diffuse radiation is measured using
 320 Kipp and Zonen 2AP sun Tracker as shown in Figure 3(b) installed at the rooftop of CSIR CEERI,
 321 Chennai, India (80°E and 13°N). Other critical parameters, such as ambient temperature and wind speed
 322 are measured using the WatchDog weather station also installed at CSIR CEERI rooftop as shown in
 323 Figure 3(c). All the measuring sensors are connected to the Keysight Data Acquisition System as shown
 324 in Figure 3(d). The details about the equipment used for experiments are given in table 6 and marked
 325 in figure 2(a).

326 Table 6 List of equipment used for the measurement

S.no.	Equipment	make	Accuracy
1	Weather station	Watch dog	
2	Pyranometer	2AP Sun Tracker	±1%
3	Pyrheliometer	2AP sun tracker	±1%
4	K-Type thermocouple		±1.6°
5	Current Shunt		±0.25%
6	MPPT	Phocos	
7	Battery	Exide (200Ah)	
8	Pump	Bajaj (18W)	
9	Flowmeter	Rotameter	±1 LPH
10	DAQ	Keysight	

327

328 3 Computational Model

329 In this section, a detailed numerical model for the desiccant-based cooling system, optical modelling of
 330 the concentrator and CFD model for the LCPVT system has been presented. For the numerical
 331 modelling of the desiccant-based cooling system, Maclain-Cross model has been utilized whereas for
 332 the optical modelling of the concentrator, ZEMAX has been used. The CFD modelling of the LCPVT
 333 system has been carried out using COMSOL Multiphysics software. Also, to capture the effect of non-
 334 uniform illumination and temperature, a coupled optical, thermal, and electrical model has been
 335 developed using MATLAB Simulink.

336 3.1 The numerical model of the desiccant-based air cooler

337 In this section, a numerical model for the desiccant-based cooling system has been discussed in detail.
 338 The desiccant wheel has been designed based on the McClain-Cross model. Further, the heat
 339 exchanger has been designed based on its effectiveness. The heating and cooling load has been
 340 calculated for both sensible and latent heat load.

341 3.1.1 The numerical model of the desiccant wheel

342 Maclain-Cross modelled heat and mass transfer of the silica gel-based desiccant wheel which is given
 343 by equation 2-3. The two processes of heat and mass transfer are given by two coupled equations which
 344 can be decoupled by introducing independent variables F_1 and F_2 where F_1 denotes constant specific
 345 enthalpy lines and F_2 denotes constant relative humidity curves in the psychrometric chart, T is the
 346 temperature of the air and W is the specific humidity of the air.

$$F_{1,k} = -\frac{2865}{(T_k + 275.15)^{1.49}} + 4.433(W_k)^{0.8624} \quad (2)$$

$$F_{2,k} = -\frac{(T_k + 275.15)^{1.49}}{6360} - 1.127(W_k)^{0.07961} \quad (3)$$

347 The intersection of the iso-potential lines provides the outlet condition of the process air in the ideal
 348 case. The real outlet condition of process air was estimated by Jurinak [43], in which two efficiency
 349 coefficients (η_{F1} , η_{F2}) as shown in equation 4-5 are also used for the calculation. In the present case,
 350 η_{F1} and η_{F2} values are assumed to be 0.08 and 0.95 respectively.

$$\eta_{F1} = \frac{F_{1,2} - F_{11}}{F_{1,8} - F_{11}} \quad (4)$$

$$\eta_{F2} = \frac{F_{2,2} - F_{21}}{F_{2,8} - F_{21}} \quad (5)$$

351

352 3.1.2 A numerical model for the sensible wheel

353 The sensible wheel or heat recovery wheel is modelled as a recuperative type heat exchanger. Equation
 354 6 [42] models the heat transfer taking place in the heat exchanger where ε is the effectiveness of the
 355 heat exchanger, T_2 is the temperature of the air after the desiccant wheel, T_3 is the temperature of the
 356 air after the sensible wheel and T_5 is the temperature of the air coming out from the room.

$$\varepsilon = \frac{T_2 - T_3}{T_2 - T_5} \quad (6)$$

357 3.1.3 Cooling coil load

358 The cooling coil load is given by equation no. 7 where as corresponding equations in terms of sensible
 359 and latent heat load of the air is given by equations 8 as mentioned in reference [44] where \dot{m} is the
 360 mass flow rate of air, C_p is the specific heat capacity of the air at constant pressure, T is the temperature
 361 of the air and w is the specific humidity of the air.

$$Q_{cc} = \dot{m}(h_3 - h_4) \quad (7)$$

$$Q_{cc} = \dot{m}C_p(T_3 - T_4) + \dot{m}h_{fg}(w_3 - w_4) \quad (8)$$

362 3.1.4 Coefficient of performance of the system

363 The coefficient of performance of the system is given by eq. 9 where Q_{coil} is the cooling load of the coil
 364 given as the sum of sensible heat load and latent heat load, P_{el} is the electrical power required by the
 365 components to run the system, Q_{LCPVT} is the thermal energy supplied by the LCPV/T system to
 366 regenerate the desiccant wheel and P_{LCPVT} is the electrical power supplied by the LCPV/T system.

$$COP_{comb} = \frac{Q_{coil}}{P_{el} - Q_{LCPVT} - P_{LCPVT}} \quad (9)$$

367

368 3.2 Optical Model

369 In the Concentrated PV/T system, optics plays a major role in enhancing the thermal and electrical
 370 performance of the system; thus, optical simulations become very important for the system design. To
 371 estimate the total radiation reaching the PV/T module via concentrator, a ray-tracing analysis is carried
 372 out using commercially available software (ZEMAX). The simulation is carried out in the non-sequential
 373 mode of the ZEMAX i.e. when the rays are launched, they interact with whatever object comes to their

374 path. Further, ZEMAX can produce child rays that take the reflected energy, and then subsequently these
375 child rays interact with whatever surfaces come in their path, and in turn produce children of their own
376 and so on. The governing equation for the law of reflection is given by equation 10 [45].

$$\vec{r}_{ref} = \vec{r}_{inc} - 2(n \cdot \vec{r}_{inc})n \quad (10)$$

377 The raytracing accounted for both Azimuth and Zenith angle tilt of the Sun. To account for azimuth and
378 zenith angle tilt in simulations using ZEMAX, Meraj et al.[46] performed a detailed analysis of the angular
379 study of the concentrator which was used in this simulation also. Further, to calculate the optical
380 concentration ratio of the concentrator, a CAD model of the concentrator is designed in Autodesk
381 inventor. The model is imported into the ZEMAX for analysis. From the CAD model, faces that help in
382 reflection is chosen as a mirror with a reflectivity of 0.95. A rectangular source of light emulating solar
383 radiation is chosen for the analysis. The number of rays is set to 10 million. The PV/T module is set as
384 a detector having 100% absorption and is divided into 100 x 100 pixels. The rays after reflection from
385 the mirror hits the absorber where the image is formed. Similarly, another detector is kept at the aperture
386 of the CPC. This detector is also divided into 100 x 100 pixels. The average pixel value of the detector
387 placed at the aperture is calculated, and then it is individually divided with each pixel of the absorber to
388 calculate the local concentration ratio on the PV/T module.

389 3.3 Thermo fluid model

390 A Thermo-Fluid model was developed to examine the heat transfer at various interfaces of the PV/T
391 module such as Glass, EVA, Solar cell, Tedlar, Aluminum sheet, copper tube, and circulating fluid. For
392 the simplicity of the model, it is assumed that all the layers of the PV panel are maintained at the same
393 temperature as the absorber plate temperature. Because of this assumption, flux can directly fall on the
394 absorber plate instead of a solar panel. Further, it is assumed that radiation emitted by the panel is not
395 radiated back to the sky. Besides, the solar radiation falling on the ECPC within the acceptance angle
396 is guided onto the PV/T module, whereas rays falling beyond the acceptance angle is reflected out of
397 the system. When the solar radiation hits the mirror profile of the CPC, losses due to reflection from the
398 mirror is observed as accounted for in the optical simulation. From the remaining part of the flux which
399 reaches the absorber, 18% of the incident flux is converted to electrical power. The remaining 82% of
400 the flux heats the absorber sheet which is subsequently dissipated to the ambient via convection loss
401 from the top and to the circulating fluid via cooling tubes in the bottom direction. Thereafter, the cell
402 temperature obtained from the thermal simulation is used to estimate the new electrical efficiency which
403 is again fed into the thermal model to estimate the new outlet and PV cell temperature. This process is
404 repeated till the outlet water temperature and cell temperature stabilizes. The process of thermal
405 simulation is shown in figure 5.

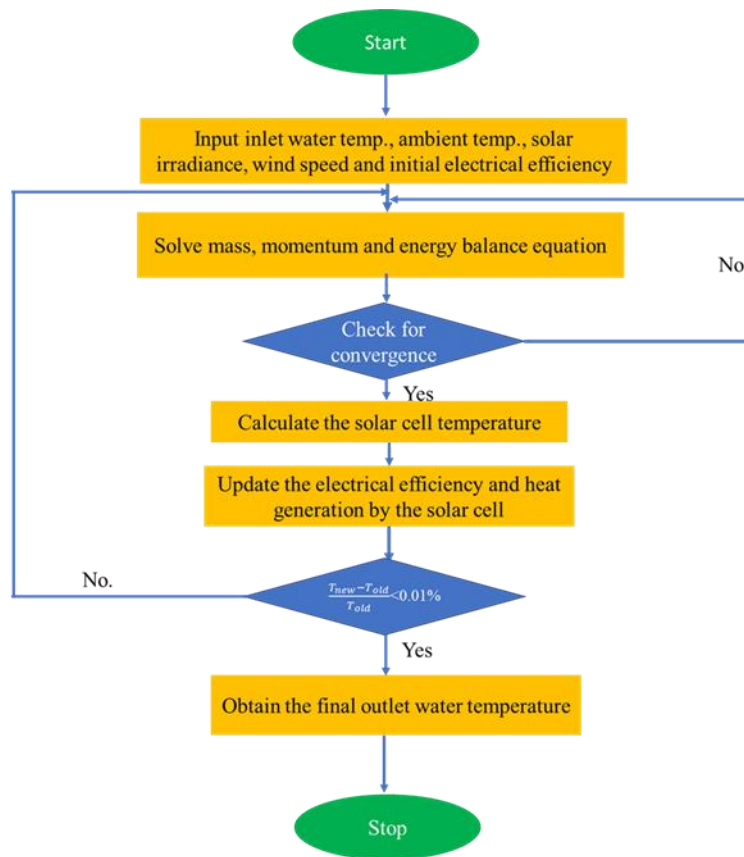


Figure 5 Flowchart for thermal simulation

406

407

408 The heat transfer at different layers of the PV/T module is modelled in commercially available finite
 409 element software (COMSOL). The geometrical model is developed as per the specification of the heat
 410 exchanger given in Table 4. On the bottom portion of the heat exchanger, the adiabatic boundary
 411 condition is used to prevent heat leakage from the PV/T module. For the water flowing inside the tube,
 412 laminar flow is considered as the flowrate inside the tube has Reynold's no. ($Re < 2300$). Reynolds no is
 413 a dimensionless no. which is a ratio of inertial force to viscous force given by equation 11 where ρ_f is
 414 the density of the fluid, V_f is the velocity of the fluid, D is the tube diameter and μ is the viscosity of the
 415 fluid.

$$Re = \frac{\rho_f V_f D}{\mu} \quad (11)$$

416

417 For the fluid domain, i.e. flow of fluid inside the heat exchanger tube, continuity, momentum, and energy
 418 equations were solved.

419 The continuity equation is given by equation 12 where V_i is the velocity of the fluid and ρ_f is the density
 420 of the fluid

$$\vec{\nabla} \cdot (\rho_f \vec{V}_f) = 0 \quad (12)$$

421

422 The momentum equation is given by equation 13 where V_f is the velocity of the fluid, ρ_f is the density
 423 of the fluid, P is the pressure of the fluid, τ is shear stress developed by the fluid and $\rho_f g$ is body force
 424 per unit area.

$$\vec{\nabla} \cdot (\rho_f \vec{V}_f \vec{V}_f) = -\vec{\nabla} P + \vec{\nabla} \tau + \rho_f \vec{g} \quad (13)$$

425 The Energy equation is given by equation 14 where ρ_f is the density of the fluid, C_p is heat capacity of
 426 the fluid, T_f is the temperature of the fluid, V_f is the velocity and K_f is the thermal conductivity of the fluid.

$$\vec{\nabla} \cdot (\rho_f C_p T_f \vec{V}_f) = \vec{\nabla} \cdot (K_f \vec{\nabla} T_f) \quad (14)$$

427 For the solid domain heat transfer equation is governed by equation 15 where K is the thermal
 428 conductivity of the fluid, q'_{gen} is heat generated by the solid

$$K_s \nabla^2 (T_s) + q'_{gen} = 0 \quad (15)$$

429 3.3.1 Fluid boundary conditions

430 At the inlet of the heat exchanger, a measured quantity of water is continuously circulated. Thus, at the
 431 inlet, the velocity of the water is a known quantity. This leads to the first boundary condition of the fluid
 432 i.e. inlet velocity which is governed by equation 16.

$$V = V_{f,in} \quad (16)$$

433 At the outlet of the heat exchanger, the pressure is set to be zero to quantify the pressure drop in the
 434 heat exchanger. This is given by equation 17.

$$P = 0 \quad (17)$$

435 At the interface of the liquid and solid, the no-slip condition is set. This is given by eq.18

$$\vec{V}_f \cdot \hat{n} = 0 \quad (18)$$

436

437 3.3.2 Thermal Boundary Conditions

438 The rays falling on the PV Panel, only part of it is converted to electricity while the rest of it is dissipated
 439 as waste heat. The waste heat generated from the solar cell can be modelled as the inward heat flux
 440 given by equation 19 where \dot{q} is the heat generated by the solar cell, $Area_{abs}$ is the area of the absorber,
 441 η_{opt} is the optical efficiency of the concentrator, S is the inward heat flux and η_{el} is the electrical
 442 efficiency of the solar cell.

$$\dot{q} = (1 - \eta_{el}) \times \eta_{opt} \times S \times Area_{abs} \quad (19)$$

443 Where electrical efficiency is a function of temperature and thus given by equation 20 where T is in °C
 444 [47], η_0 is the base efficiency of the solar cell, and β is the rate of degradation of the solar cell.

$$\eta_{el} = \eta_0 (1 - \beta(T - 25)) \quad (20)$$

445 Since the heat generation takes place in solar cells, it is conducted to the top portion of the PV panel
 446 and then lost to ambient via convection heat transfer as given by Equations 21 and 22 . Thus, on the
 447 top face of the PV/T module, convective heat transfer boundary condition is set where h_{conv} is the
 448 convective heat transfer coefficient and u is the wind speed.

$$h_{conv} = 2.8 + 3u \quad (21)$$

$$Q_{conv} = h_{conv}(T - T_{amb}) \quad (22)$$

449 Similarly, on the bottom and a side portion of the PV/T module, the adiabatic boundary condition is set,
 450 i.e. no heat loss takes place from the bottom side of the heat exchanger. For the fluid domain, at the
 451 inlet of the heat exchanger, the inlet water temperature is specified as a boundary condition.

452 3.4 Electrical Model

453 The PV cell can be modelled as a current generating source having a diode and a resistor each
 454 connected in parallel to it. An additional resistor is connected to the circuit in series as shown in Figure
 455 6. The I-V characteristic curve for the PV panel is governed by equation 23 [35] where I is the current
 456 generated by the PV cell, I_0 is diode current, I_l is the light generated current, V is the voltage developed
 457 by the solar cell, R_s is series resistance accounting for resistance caused due to improper contact, n is
 458 diode factor, α is the thermal voltage given by equation 24 and R_{sh} is shunt resistance accounting for
 459 crystallographic and manufacturing defect in the solar cells. For solving the electrical model, the five-
 460 parameter model is selected from the MATLAB Simulink to estimate the performance of the PV panel
 461 subjected to concentration. At first, the reference value of I_l , I_0 , R_s and R_{sh} are calculated for 1000 W/m²
 462 and 25°C referred as $I_{l,ref}$, $I_{0,ref}$, $R_{s,ref}$ and $R_{sh,ref}$. Thereafter the values of I_l , I_0 , R_s and R_{sh} are calculated
 463 for the actual irradiance and actual operating temperature during concentration which is given by
 464 equation 24-28.

$$I = I_l - I_0 \left(\exp \left(\frac{V + IR_s}{n\alpha} \right) - 1 \right) - \frac{V + IR_s}{R_{sh}} \quad (23)$$

$$\alpha = \frac{K_t T}{q_c} \quad (24)$$

465 The temperature plays a significant role in the thermal voltage developed by the solar cells. The thermal
 466 voltage α is directly proportional to the temperature T in K. and Stefan Boltzmann constant K. The
 467 thermal voltage is inversely proportional to the charge of the electron. The thermal voltage is given by
 468 equation 24 [35]. Since K and q_c are constant values. Therefore the equation 24 converts to equation 25
 469 for a temperature higher than operating temperature.

$$\frac{\alpha}{\alpha_{ref}} = \frac{T}{T_{ref}} \quad (25)$$

470 Thereafter, the effect of irradiance on light generated current is solved which is given by equation 26
 471 [35] where I_l is the light generated current developed by the solar cell at any irradiance value G, G_{ref} is
 472 the reference irradiance value, μ_{isc} is the degradation rate of the cell due to current, T is the operating
 473 temperature of the solar cell and T_{ref} is the reference temperature of the solar cell.

$$I_l = \frac{G}{G_{ref}} [I_{l,ref} + \mu_{isc} (T - T_{ref})] \quad (26)$$

474 Similarly, the variation of diode current with temperature and irradiance is given by equation 27 [35]
 475 where I_0 is the diode current at any temperature, $I_{0,ref}$ is the diode current at the reference temperature,
 476 N_s is the no of solar cells connected in series and ϵ_{sc} is the bandgap of the solar cell.

$$\frac{I_0}{I_{0,ref}} = \left(\frac{T}{T_{ref}} \right)^3 \exp \left[\frac{\epsilon_{sc} N_s}{\alpha_{ref}} \left(1 - \frac{T_{ref}}{T} \right) \right] \quad (27)$$

477 Further, it is assumed in this model that the series resistance of the solar cell remains unaffected due
 478 to the increase in temperature whereas the shunt resistance is inversely proportional to the irradiance
 479 falling on the solar cell is given by equation 27 [35] and 28 [35] respectively.

$$R_s = R_{s,ref} \quad (28)$$

$$R_{sh} = \frac{G_{ref} R_{sh,ref}}{G} \quad (29)$$

480 In the present case, the equation no 23-29 are solved in MATLAB-Simulink for each of the solar cells in
 481 the PV panel for the different values of irradiance as obtained from the ZEMAX simulation and different
 482 values of temperature as obtained from the COMSOL simulation.

483

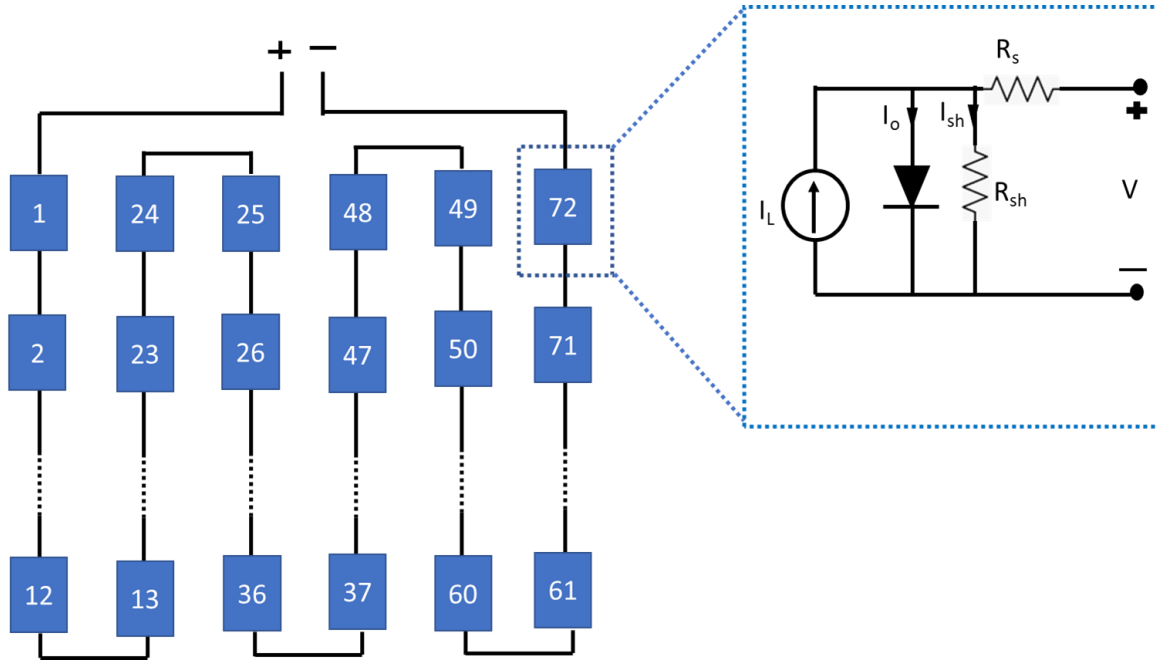


Figure 6. Arrangement of 72 cells connected in series in 12 rows and 6 columns

484 3.5 Error analysis

485 The reliability of the experiments depends on the accuracy of the instruments and systems used in the
 486 experiments. The uncertainty analysis quantifies the accuracy of the experimental data. The uncertainty
 487 associated with the measurement in thermal and electrical measurements is given by equations 30-33
 488 [48] which comes out to be 8% for thermal measurement and 2% for electrical measurement.

$$\eta_{th} = \frac{\dot{m}C_p(T_{out} - T_{in})}{(CI_b + I_d).A} \quad (30)$$

$$\eta_{th} = \frac{V_{mp}I_{mp}}{(CI_b + I_d).A} \quad (31)$$

$$\Delta \eta_{th} = \sqrt{\left(\frac{\partial \eta_{th}}{\partial m} \Delta m\right)^2 + \left(\frac{\partial \eta_{th}}{\partial T_{in}} \Delta T_{in}\right)^2 + \left(\frac{\partial \eta_{th}}{\partial T_{out}} \Delta T_{out}\right)^2 + \left(\frac{\partial \eta_{th}}{\partial I} \Delta I\right)^2} \quad (32)$$

$$\Delta \eta_{ele} = \sqrt{\left(\frac{\partial \eta}{\partial V_{mp}} \Delta V_{mp}\right)^2 + \left(\frac{\partial \eta}{\partial I_{mp}} \Delta I_{mp}\right)^2 + \left(\frac{\partial \eta}{\partial I} \Delta I\right)^2} \quad (33)$$

489

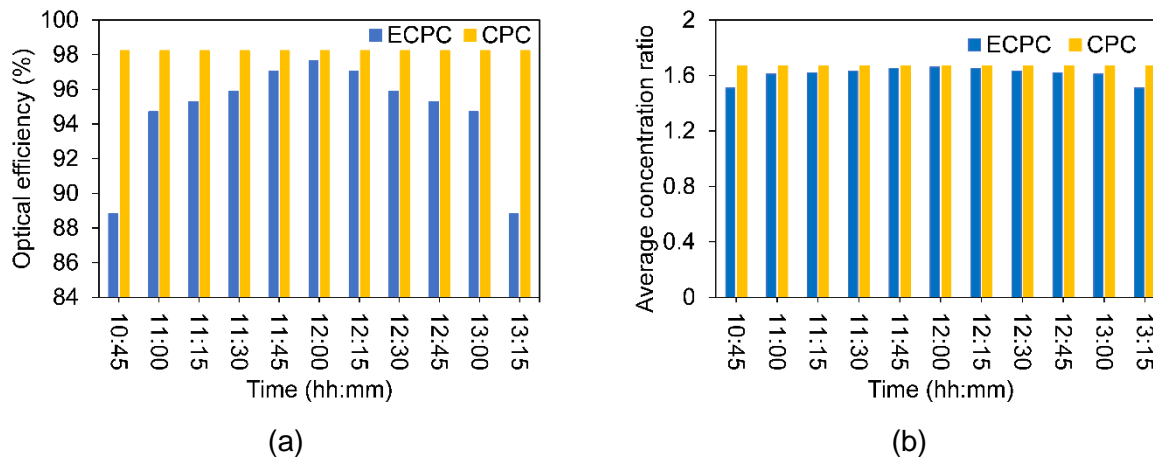
490 4 Results and discussion

491 In this section, a coupled optical, electrical, and thermal model is developed. Simulations are carried
 492 using the coupled model to predict the thermal performance of the system. After that, a comparison
 493 between thermal simulations and experiments are carried out to validate the model. After validation of

494 the model, thermal simulations are extended to the CPC-based LCPV/T system also for comparing the
 495 performance of both systems. Finally, the optical flux obtained from the ZEMAX and thermal simulation
 496 results obtained from the COMSOL model is extracted and then used as input to the electrical model
 497 developed in MATLAB-Simulink for predicting the electrical performance of the system.

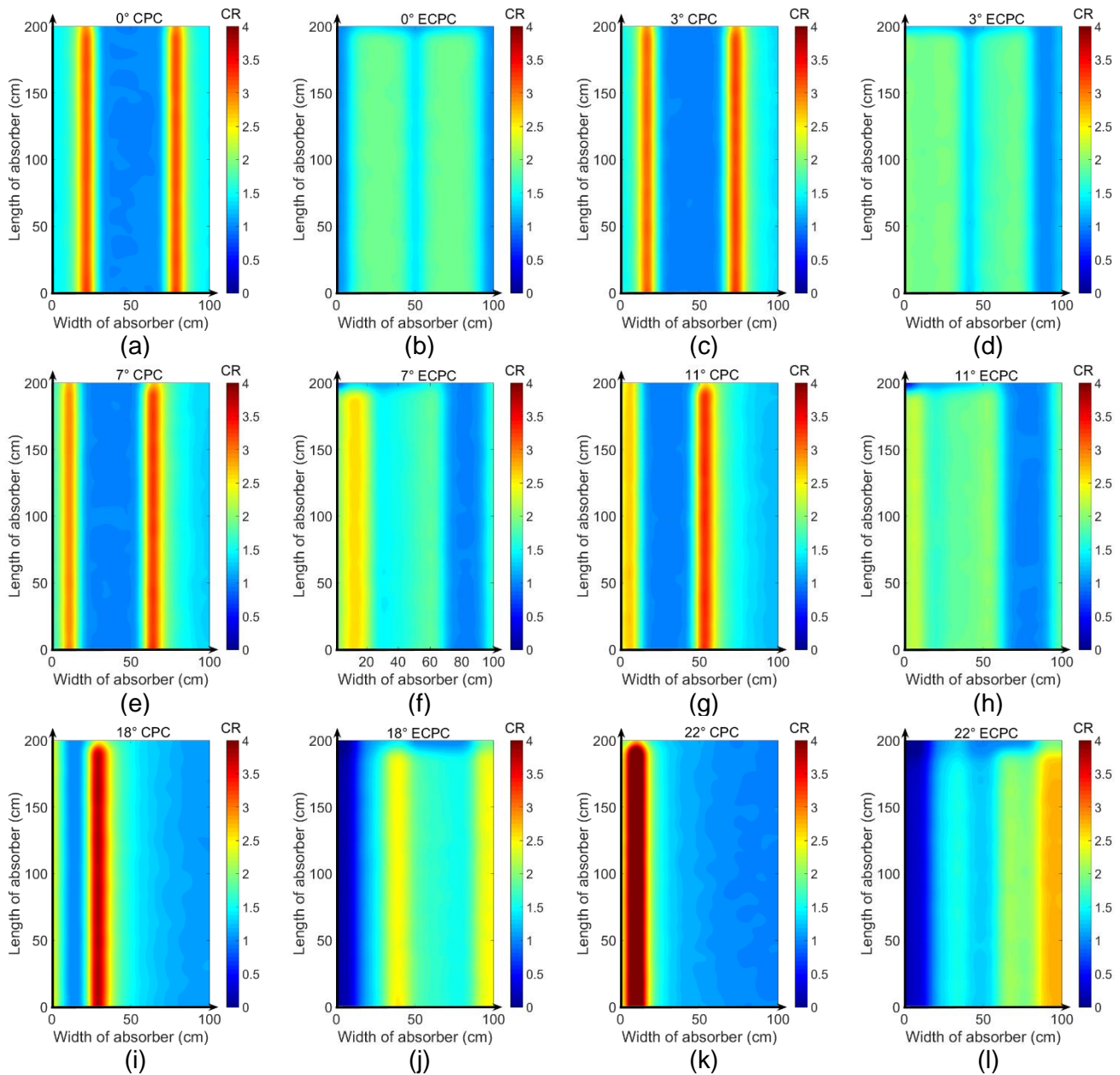
498 4.1 Optical simulation results of Low Concentrating Photovoltaic Thermal system

499 Figure 7(a) shows the variation of optical efficiency of the concentrator with time on 28th September
 500 2019. The declination angles of the Sun on 28th September is observed to be 3°. The optical efficiency
 501 for the case of CPC, at 12 pm or 0° the incidence angle is observed to be 0.98 whereas for the case of
 502 ECPC it is observed to be 0.97. The optical efficiency of the ECPC largely depends on the angle of
 503 incidence of the Sun. As the angle of incidence of the sun increases, no. of rays hitting the homogenizer
 504 also increases resulting in lower optical efficiency. Compared to ECPC, the optical efficiency of the CPC
 505 largely remains constant at all angles of incidence however, the spatial non-uniformity sharply increases.
 506 Similarly, Figure 7(b) shows the variation of the average concentration ratio for the CPC and ECPC
 507 based concentrators. As the CPC has higher optical efficiency compared to the ECPC, the average
 508 concentration ratio is also observed to be higher.



509 Figure 7 (a) Variation of optical efficiency of the CPC and ECPC with time when declination angle of
 510 Sun is 3° (b) Variation of optical concentration ratio of the CPC and ECPC with the angle of incidence
 511 when the declination angle of Sun is 3°

512 The flux profile of the CPC and ECPC is shown in Figures 8(a-l). As the incidence angle increases, the
 513 flux falling on the CPC also tends to shift in the same direction as that of the incidence angle, reaching
 514 a maximum (4x) near the acceptance angle. For the case of ECPC, the additional optical component
 515 called homogenizer reduces the severity of the local concentration significantly. However, beyond the
 516 15° angle of incidence, the homogenizer tends to cast a shadow on the PV/T module, which has a
 517 detrimental effect on the electrical performance of the system which will be explained in the coming
 518 sections.



519

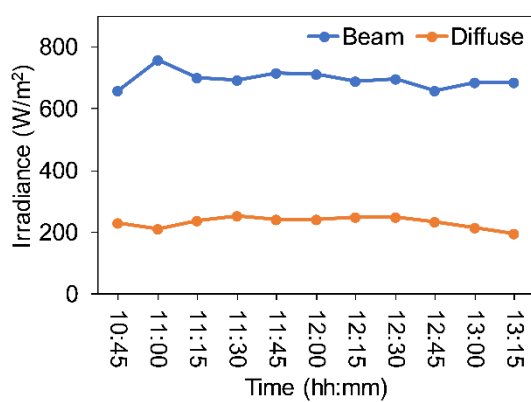
520 Figure 8 (a) Flux formed on the absorber due to CPC at 0° (b) ECPC 0° (c) CPC 3° (d) ECPC 3° (e)
 521 CPC 7° (f) ECPC 7° (g) CPC 11° (h) ECPC 11° (i) CPC 18° (j) ECPC 18° (k) CPC 22° (l) ECPC 22°

522 **4.2 Thermal simulation and experiment results of Low Concentrating Photovoltaic**
 523 **Thermal system**

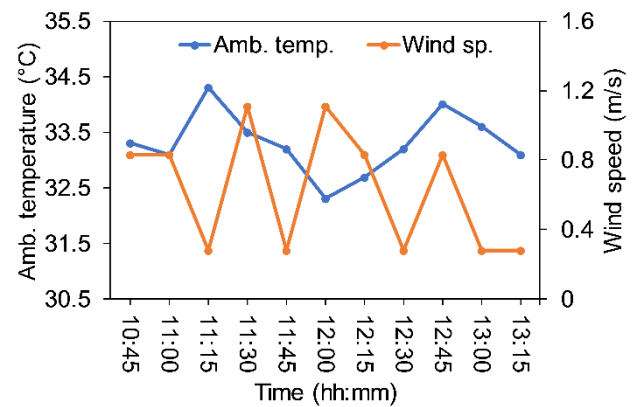
524 In this section, the results of the thermal simulation of the LCPV/T system have been reported. The
 525 outlet water temperature from the LCPV/T system is a strong function of solar irradiance, wind speed,
 526 and ambient temperature. For thermal analysis of the LCPV/T system, all the meteorological data were
 527 collected on 28th September 2019. Figure 9(a) shows the variation of the beam and diffuse irradiance
 528 falling on the LCPV/T system on 28th September 2019. The peak beam radiation was observed to be
 529 756 W m⁻², and corresponding diffuse radiation was observed to be 212 W m⁻² at 11 am. Figure 9 (b)
 530 shows the variation of wind speed and ambient temperature on 28th September 2019. The average

531 beam radiation, diffuse radiation, ambient temperature, and wind speed was recorded to be 695 W m⁻²,
 532 238 W m⁻², 33.3° C, and 0.64 m/s respectively

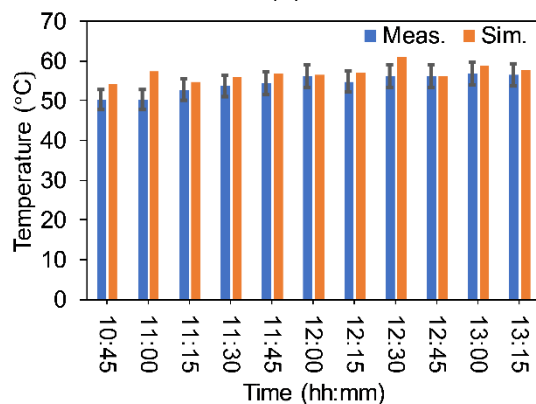
533 The results for the comparison of thermal simulations and experiments carried out on 28th September
 534 2019 at 24 LPH is shown in Figure 9(c). From the figure, it is observed that the outlet water temperature
 535 is around 46.7 °C at around 10:45 AM. The low outlet water temperature can be attributed to the low
 536 inlet water temperature and low optical efficiency (88%) of the concentrator. However, at around 11 am
 537 or -15° angle of incidence, a considerable difference between simulation and experiments were
 538 observed where the simulated outlet water temperature was observed to be 57°C while the measured
 539 outlet water temperature was observed to be 50°C. This discrepancy between simulation and
 540 experiments can be attributed to increased optical efficiency of the concentrator (94%) and low wind
 541 speed resulting in less dissipation of heat from the top direction. At other angles of incidence, a close
 542 match between simulations and experiments was observed with peak outlet water temperature
 543 measured to be 56°C at noon. Besides, the overall relative error between simulations and experiments
 544 was reported to be under 6%. Figure 9(d) shows the variation of thermal efficiency with time. The
 545 thermal efficiency of the system is observed to be around 36% experimentally. The thermal efficiency
 546 of the LCPV/T system is calculated using equation 30.



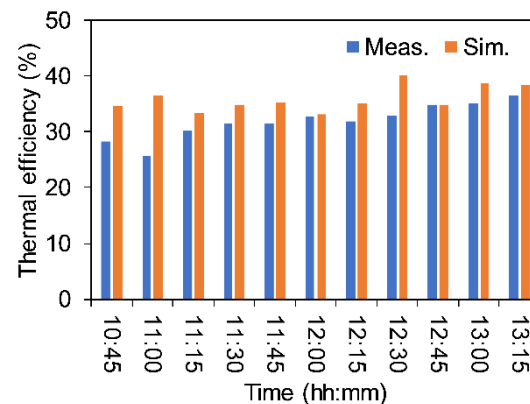
(a)



(b)



(c)

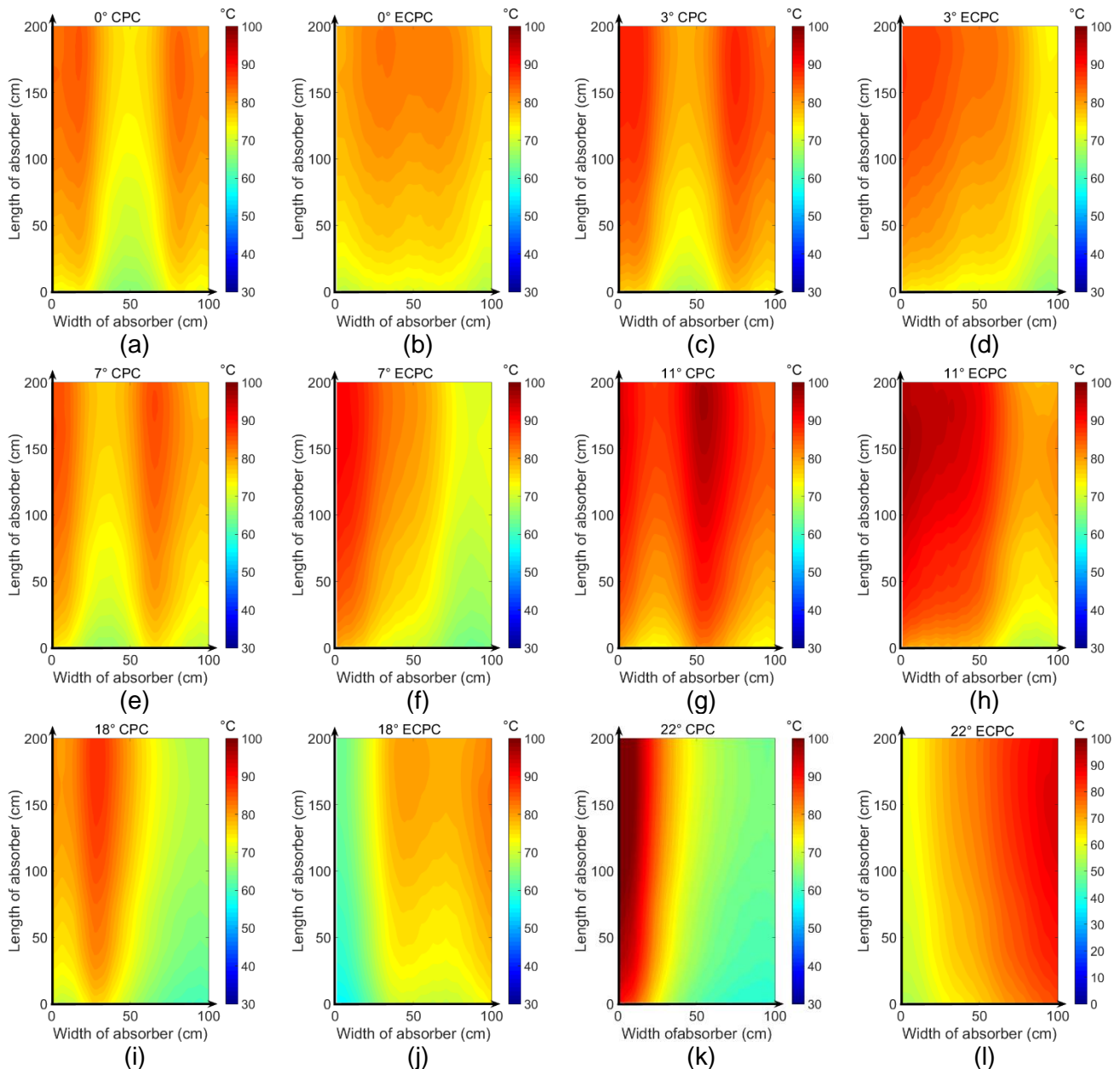


(d)

547 Figure 9 (a) variation of the beam and diffuse radiation with time on 28th September 2019 (b) variation
 548 of wind speed and ambient temperature on 28th September 2019 (c) variation of outlet water temperature
 549 with time (d) variation of thermal efficiency with time

550 Further, the thermal simulation data is analyzed for 28th September 2019 between 10:30 am or 22° angle
 551 of incidence and noon 0° angle of incidence for both the cases of CPC and ECPC. The flux obtained
 552 from the optical simulation of the CPC and ECPC is used as input flux on the thermal simulation. The

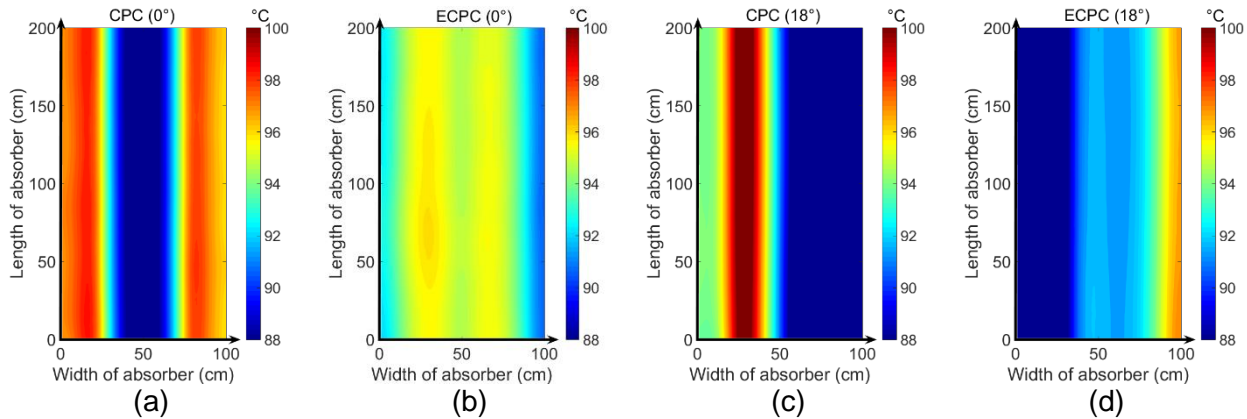
553 temperature distribution on the surface of the PV/T module is shown in Figure 10 (a-l). As expected, in
 554 the region where the optical flux is more concentrated on the PV/T module, a higher panel temperature
 555 is observed. Near the half acceptance angle of the concentrator, the localized heating in the case of
 556 CPC dominates resulting in the temperature of $\sim 100^{\circ}\text{C}$, whereas, in the case of ECPC, the temperature
 557 is well below 80° . It can be concluded that the non-uniformity in illumination on the PV/T module caused
 558 due to the CPC results in the formation of hot spots which brings down the life of the PV panel
 559 significantly.



560 Figure 10 Temperature distribution on the absorber due to (a) CPC at 0° (b) ECPC 0° (c) CPC 3° (d)
 561 ECPC 3° (e) CPC 7° (f) ECPC 7° (g) CPC 11° (h) ECPC 11° (i) CPC 18° (j) ECPC 18° (k) CPC 22° (l)
 562 ECPC 22°

563 Figure 11 shows the variation of temperature on the solar panel when the panel is subjected to
 564 concentration without cooling condition or stagnation condition. Figure 11(a) shows the variation of
 565 temperature for the case of CPC at a 0° angle of incidence. The figure shows that, due to non-uniform
 566 illumination, there is a formation of a hot spot on the column of the solar cells. These hotspots can

567 potentially degrade the solar cells at a much faster rate compared to the case of the ECPC based
 568 LCPV/T system where temperature distribution is more uniform. For the case of CPC (0°), there is a
 569 difference in temperature between cells operating at maximum and minimum temperature of about 10-
 570 12°C . This huge thermal gradient can potentially reduce electrical performance in long run. As the angle
 571 of incidence increases, the non-uniform distribution of flux caused due to CPC on the PV panel further
 572 increases. Near the half acceptance angle, the localized heating of the solar panel dominates as shown
 573 in Figure 11(c). This can further enhance the degradation of the solar cells at a much faster rate failing
 574 the solar panel.

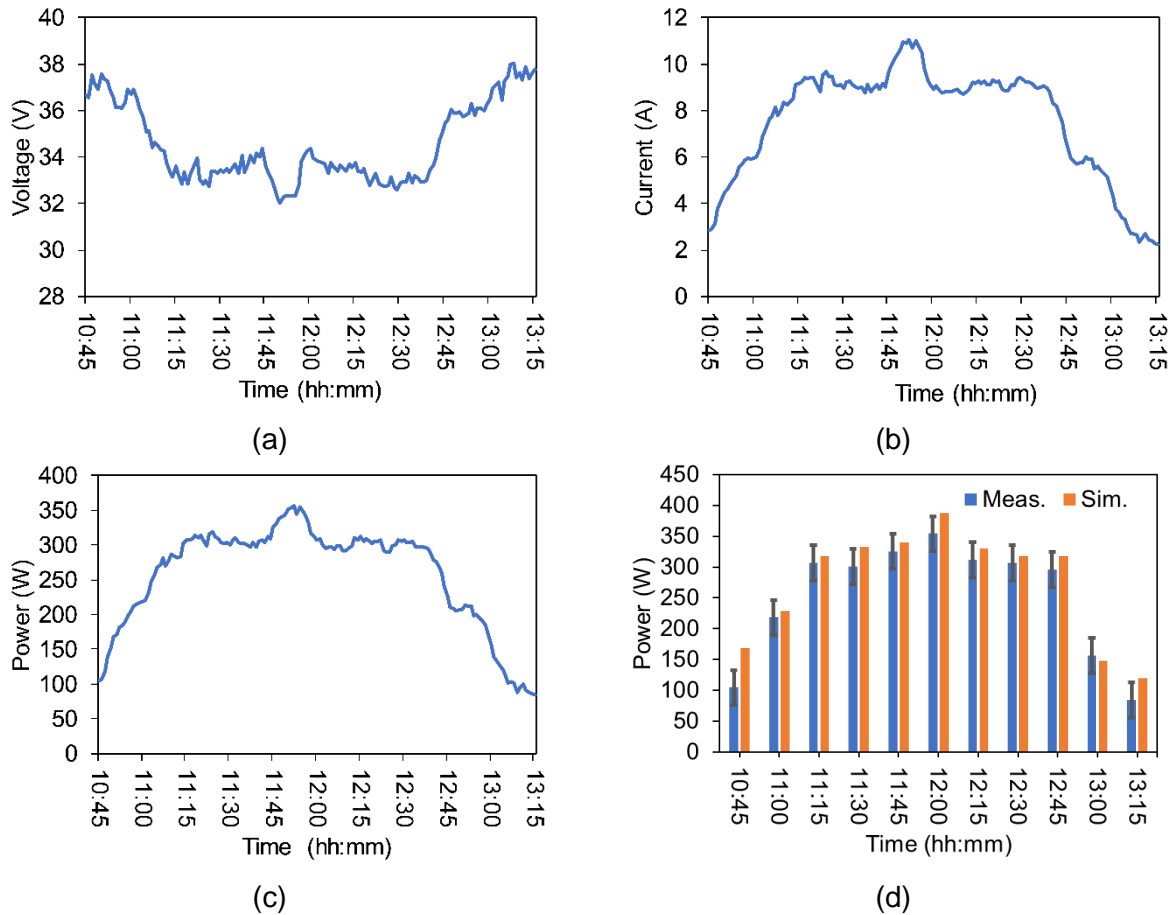


575 Figure 11 Temperature distribution on the PV panel for the stagnation condition (a) 0° CPC (b) 0°
 576 ECPC (c) 18° CPC (d) 18° ECPC

577 4.3 Electrical simulation and experiment results of Low Concentrating Photovoltaic 578 Thermal system

579 The electrical simulations and experiments were carried out for the ECPC on 28th September 2019. On
 580 28th September 2019, a 380 W PV panel was integrated into the LCPV/T system. Figure 12(a) shows
 581 the variation of experimentally obtained voltage with time. At 10:45 am, the voltage is observed to be in
 582 the range of 36-38V. The high voltage in the PV panel can be attributed to the lower operating
 583 temperature of the solar cells. As the angle of incidence increases, the flux reaching the absorber area
 584 also increases resulting in higher operating temperatures. The higher operating temperature
 585 subsequently leads to a dip in voltage. At noon, the voltage is measured to be around 32 V. Figure 12(b)
 586 shows the variation of current with time. At 10:45 am, the current is observed to be ~ 3 A. The low current
 587 value can be explained from the optical simulation results of the ECPC at an 18° angle of incidence
 588 where the homogenizer is casting a shadow on the PV panel area resulting in lower electricity
 589 generation. As the day progresses, the angle of incidence decreases resulting in better distribution of
 590 flux and improved electricity generation from the panel. At around noon the peak current was measured
 591 to be ~ 11 A. Figure 12(c) shows the variation of power output from the PV panel with time. The peak
 592 power is observed to be 357 W when the angle of incidence is observed to be 0° . Thereafter, the
 593 electrical simulation is carried out to validate the electrical model with experiments as shown in Figure
 594 12(d). The electrical simulations are coupled with optical and thermal simulations. The coupling is done
 595 by dividing the flux obtained from the optical simulation and temperature profile obtained from thermal
 596 simulations into a matrix of 12×6 configuration. Each cell in the matrix represented the average flux and
 597 average temperature of the solar cell. These optical and thermal fluxes are used as input to the PV
 598 panel designed in MATLAB-Simulink. At 12 pm or 0° angle of incidence, the electrical power output of
 599 357W is measured, whereas the simulated peak power is observed to be 380W for the same angle of
 600 incidence. The improved electrical output from the ECPC based concentrator at a 0° angle of incidence
 601 is attributed to the uniform distribution of flux on the PV panel area. Thereafter, at higher angles, i.e.
 602 beyond 10° or after 11:15 am, a significant drop in electrical power is observed for ECPC. The significant

603 decrease in electrical power output is mainly because of the homogenizer casting shadow on the column
 604 of the solar cell. Overall, a close match between simulation and experiments were observed with some
 605 deviations at 10:45 am and 1:15 pm.

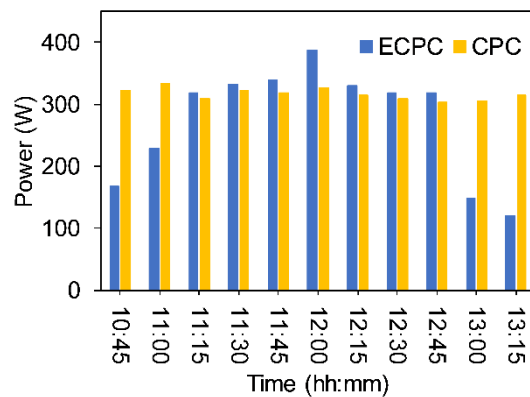
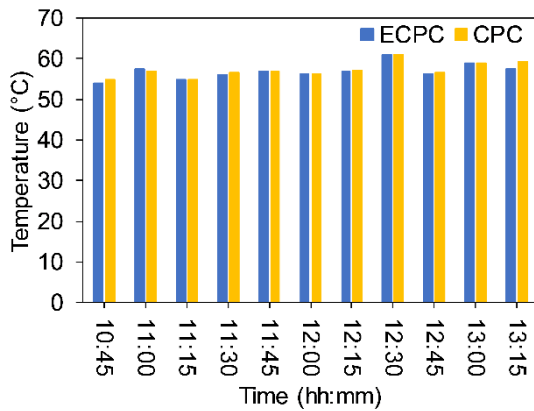


606 Figure 12 (a) Variation of voltage with time (b) Variation of current with time (c) Variation of Power with
 607 time (d) Comparison between measured and simulated electrical power electrical power

608 4.4 Comparison between Compound Parabolic Concentrator and Elongated 609 Compound Parabolic Concentrator

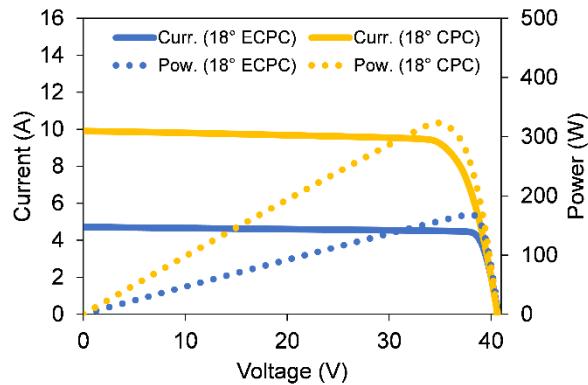
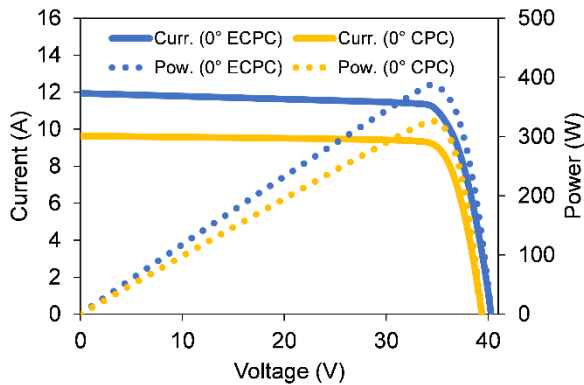
610 To study the advantage of the homogenizer integrated into the CPC, a comparative study of the thermal
 611 and electrical performance of the CPC and ECPC based LCPV/T system is conducted. Simulations are
 612 carried when the Sun declination angle is observed to be 3°. Figure 13(a) shows the comparison
 613 between thermal simulations of the CPC and ECPC. From the simulation, it is observed that the outlet
 614 water temperature is nearly the same. However, due to the higher concentration ratio of the CPC, a
 615 slight improvement of ~0.2°C outlet water temperature is observed. After that, a comparative study of
 616 the electrical simulation is also carried out as shown in Figure 13(b). Results show that, for the case of
 617 CPC, despite having higher optical efficiency, the electrical power output is lower compared to the
 618 electrical power output of the ECPC. The higher electrical power output of ~12% at a normal angle of
 619 incidence is attributed to the uniform distribution of flux in the case of ECPC compared to CPC. However,
 620 with an increase in the angle of incidence, the difference between the electrical output from the CPC
 621 and ECPC reduces. Beyond a 10° angle of incidence or 11:15 am, the electrical power output from the
 622 CPC overtakes the electrical power output from the ECPC. The prime reason for the sudden decrease
 623 in electrical power output can be attributed to the shadow cast by the homogenizer on the PV panel as
 624 observed in optical simulation results also. Figure 13(c) shows the variation of current and power
 625 generated by the CPC and ECPC based LCPV/T system at 0° angle of incidence. For the case of ECPC,

626 a maximum current of 11.37 A is observed whereas, for the case of CPC, the maximum current of 9.2
 627 A is observed. The higher current is attributed to the better distribution of flux as observed in the case
 628 of ECPC compared to CPC of the same geometrical configuration. Figure 13(d) shows the variation of
 629 current and power for the case of CPC and ECPC at an 18° angle of incidence. For the case of ECPC,
 630 as explained earlier, the homogenizer shadow falling at the edges of the PV panel reduces the electricity
 631 generation whereas, for the case of CPC, the whole PV panel is illuminated resulting in higher electricity
 632 generation. The maximum current in the case of CPC is observed to be ~10A whereas for the case of
 633 ECPC it is observed to be ~4A. The power developed by the CPC is observed to be around 300W
 634 whereas for the case of ECPC, the power developed is around 170W only. Even though the power
 635 developed by the CPC-based LCPV/T system is higher beyond the certain angle of incidence compared
 636 to the ECPC based LCPV/T system, the severity of the non-uniform distribution of flux also increases.
 637 This results in the formation of hot spots on the solar cells. These hotspots not only affect the overall
 638 electrical efficiency of the solar cells but also induces thermal fatigue caused due to temperature
 639 gradient.



(a)

(b)



(c)

(d)

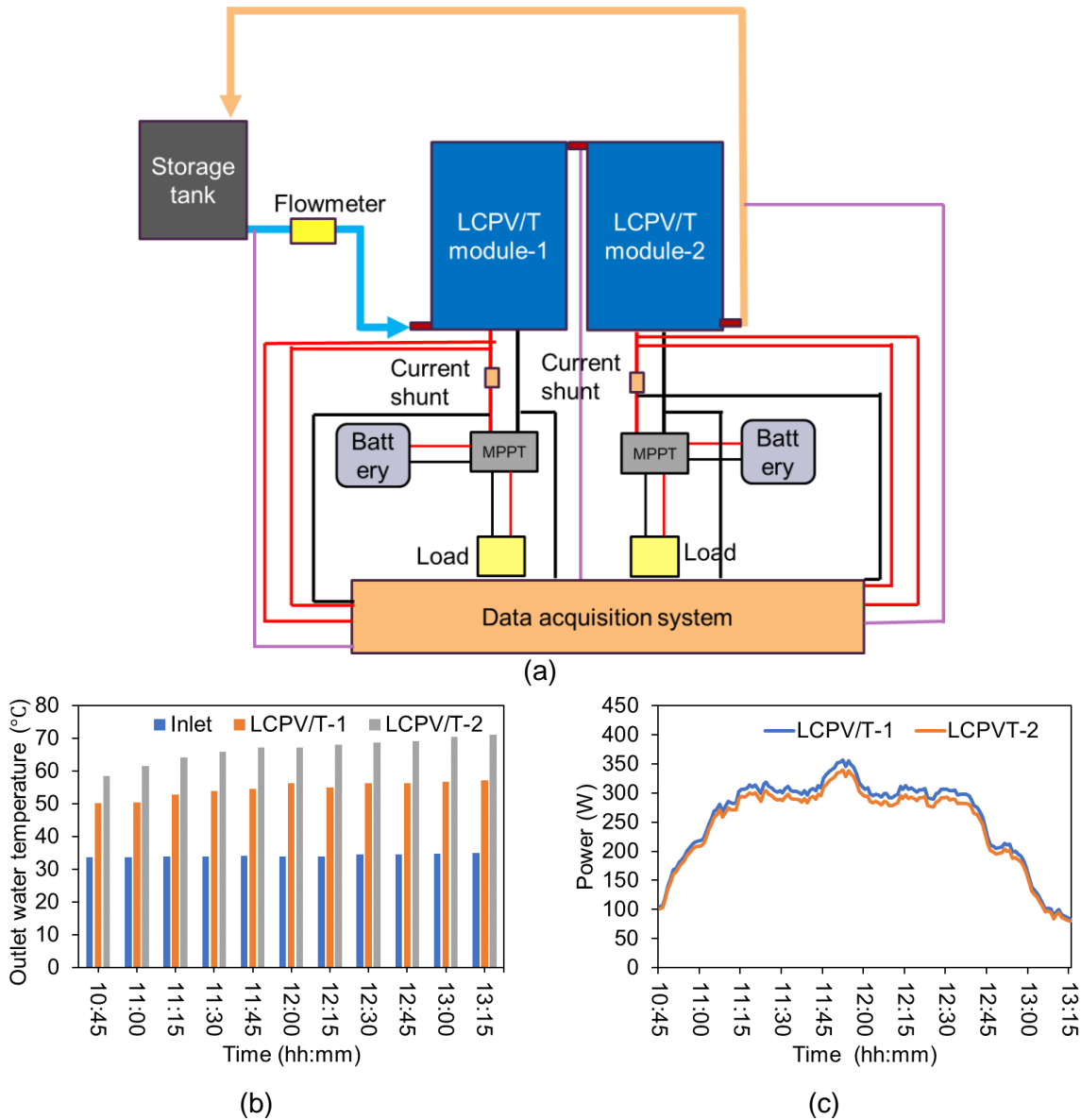
640 Figure 13 (a) Variation of thermal output from the CPC and ECPC on 28th September (b) Variation of
 641 electrical output from the CPC and ECPC on 28th September (c) Variation of current and power at 0°
 642 angle of incidence (d) Variation of current and power at 18° angle of incidence.

643 4.5 Outputs using two series connected Low concentrating Photovoltaic Thermal

644 To improve the grade of thermal output, two LCPVT system needs to be connected in series to meet
 645 the temperature requirement. The experimental results of the series-connected systems are shown in
 646 Figure 14. Results show that, when two LCPVT systems are connected in series, the outlet water
 647 temperature is observed to be in the range of 60-70°C which indicates that, it can meet the requirement
 648 of regenerating the desiccant wheel. Also, it was noted that the electrical power output of the 1st panel

649 was 4.5% more compared to the second panel. The decrease in power output from the second panel
 650 was noted mainly because of the high operating temperature of the second panel. Figure 14(c) shows
 651 the electrical output from two solar panels of two different LCPVT systems. The electrical connections
 652 for the two systems were made independent of each other to ensure that one system electrical power
 653 is not affected by the other system's electrical power. Additional experimental results at different flowrate
 654 and weather conditions have been provided in the supplementary information.

655

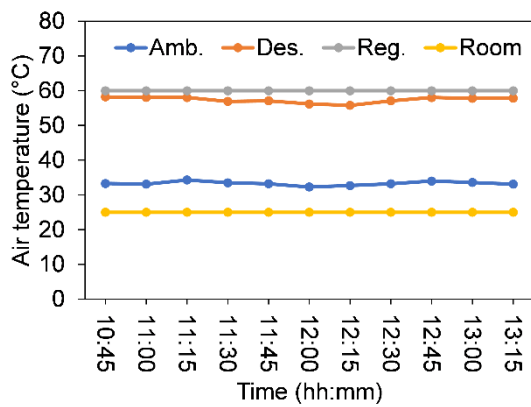


656 Figure 14 (a) Schematic of the series-connected LCPVT system (b) outlet water temperature from the
 657 series-connected system (c) electrical power output from the series-connected system.

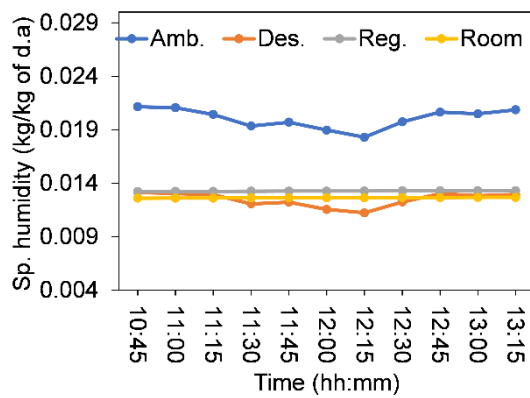
658 4.6 Performance of the desiccant-based air conditioning system

659 The designed series-connected LCPV/T system is then coupled with the desiccant-based air conditioning
 660 system. The simulation for the desiccant-based air conditioning system is carried out using
 661 MATLAB for 28th September 2019 data. The results are shown in Figure 15. As shown in Figure 15 (a),
 662 the ambient temperature is ~32°C, the supply air after passing through the desiccant wheel is ~55°C,
 663 the sensible cooling of the supply air after passing through the sensible wheel is ~33°C and the

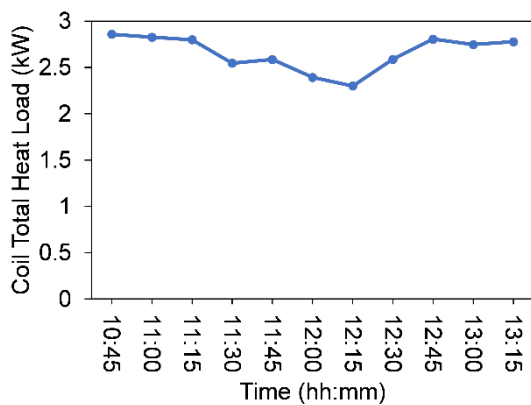
664 regeneration temperature is assumed to be constant at 60°C. Figure 15 (b) shows the variation of
 665 specific humidity of the air with time. For the ambient air, the specific humidity is observed to be 0.020
 666 kg/ kg of d.a. After the air passes through the desiccant wheel, a reduction in moisture content is
 667 observed. The moisture content of the air after dehumidification is observed to 0.012 kg/kg of d.a. When
 668 the air enters the room, due to the latent heat load of the room an increase in specific humidity is
 669 observed. Figure 15 (c) shows the variation of coil total heat load. The average coil heat load is observed
 670 to be 2.5 kW. At around 11:15 am and 12:45 pm a dip in coil load is observed. This dip in coil total heat
 671 load is mainly because of the lower specific humidity of the air as shown in Figure 15 (b). Figure 15 (d)
 672 shows the variation of the compressor power. The average compressor power for the simulation is
 673 observed to be 0.6kW. Further, it is observed that the compressor power followed a similar trend as
 674 observed in the case of coil total heat load with a dip in compressor power between 11:15 am and 12:45
 675 pm. Figure 15 (d,e) shows the variation of COP and EER of the compressor with time. As observed from
 676 the simulations, the integration of the LCPV/T system to the desiccant-based air cooler improves the
 677 COP of the system by ~50%. Results also showed improvement in COP for the case of ECPC based
 678 LCPV/T over the CPC-based LCPV/T system between 11:15 am and 12:45 pm reaching a maximum of
 679 up to 5% at a normal angle of incidence.



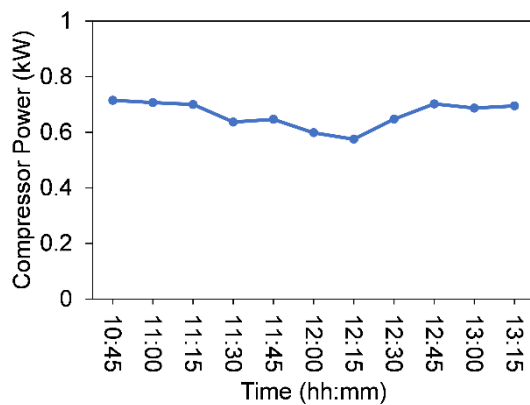
(a)



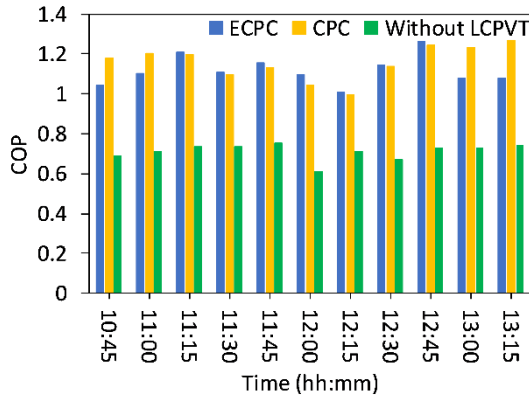
(b)



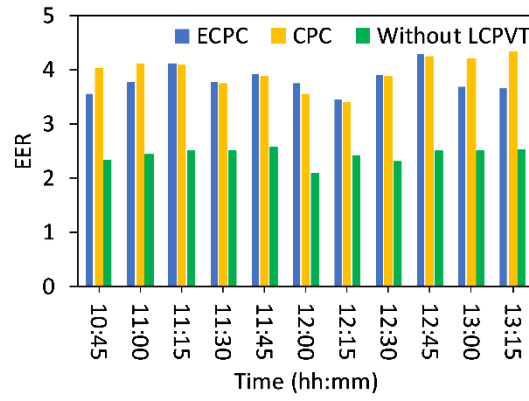
(c)



(d)



(e)



(f)

680 Figure 15 Variation of (a) temperature of the air (b) specific humidity of the air (c) coil total heat load
 681 (d) compressor power (e) COP with the angle of incidence (f) EER with the angle of incidence
 682

683 4.7 Cost-benefit analysis

684 In this section, a techno-economic analysis of mass production of the system is carried out. Besides,
 685 techno-economic analysis, the environmental impact of the installation of such an LCPV/T system is
 686 also carried out. In this analysis, the only cost of the components is considered whereas the
 687 maintenance and installation charges are neglected.

688 4.7.1 Cost comparison with PV panel

689 The cost of the components used in the 1 unit of LCPV/T system having peak electrical output of 357
 690 W_e and peak thermal output of 622 W_{th} are shown in Table 7. The total cost for each module of the
 691 LCPV/T system comes out to be INR. 32175 (considering bill of material). Whereas the cost of the
 692 system per m^2 is observed to be INR. 9500/ m^2 where the aperture area of the LCPV/T system is 3.4 m^2 .
 693 Thereafter the cost comparison for the PV panel is carried out for the cost comparison of the LCPV/T
 694 system. In the present case, the cost of a monocrystalline PERC solar panel of 380W capacity was
 695 purchased for INR.10,000. Therefore, the cost of the module is observed to be INR. 26/ W_e as given by
 696 equation 30. Similarly, the cost of the LCPV/T module is also calculated with peak electricity generation
 697 of 357 W_e (experimental results) and peak thermal energy generation of 622 W_{th} (experimental results)
 698 which comes out to be INR. 90/ W_{el} and INR. 24/ W_{th} as given by equation 35-36 [41].

$$699 \text{ Cost of electrical output from only PV panel } \frac{Rs}{W} = \frac{\left(\frac{10000}{2}\right)}{\left(\frac{380}{2}\right)} = 26 \quad (34)$$

$$700 \text{ Cost of electrical output from LCPVT system } \frac{Rs}{W} = \frac{\left(\frac{32175}{3.4}\right)}{\left(\frac{357}{3.4}\right)} = 90 \quad (35)$$

$$701 \text{ Cost of thermal output in LCPVT system } \frac{Rs}{W} = \frac{\left(\frac{32175}{3.4}\right) - \left(\frac{10000}{2}\right)}{\left(\frac{622}{3.4}\right)} = 24 \quad (36)$$

699 Table 7: Cost of equipment

Component	Cost (INR.)
Aluminium sheet	3025
Copper tube	1150

Glass wool	1000
Concentrator (Aluminum reflectors)	7000
Structure	10,000
PV panel	10,000

700 4.7.2 Energy savings of the LCPV/T system

701 For the calculation of thermal and electrical energy yield from the LCPV/T system. Experiments were
702 conducted on 28th September 2019. From the experiments, the total energy generated by the LCPV/T
703 system over a day is calculated which comes out to be 0.75 kWh_e/Day and 1.15 kWh_{th}/ day. It is assumed
704 that the system will generate the same energy for 250 days. Therefore, the yearly yield from the system
705 is observed to be 187 kWh_e/yr and 287 kWh_{th}/yr. Similarly, the energy generated by the system for the
706 whole year per meter sq. area is observed to be 55 kWh_e/(m² yr) and 84 kWh_e/(m² yr) where an aperture
707 area of 3.4 m² is considered for the calculation.

708 Further, the estimation of natural gas savings by the installation of the LCPV/T system is calculated.
709 Since the system generates both electrical and thermal power from the same system and grade of
710 energy developed is different. It is decided to convert the electrical energy to equivalent thermal energy
711 by a conversion factor of 0.38[41] and then estimate the natural gas savings. The equation (37-38) [41]
712 used for the calculation of natural gas savings comes out to be 4.9 therms/ (m² year) and 2.9 therms/(m²
713 year).

$$NG_{saved\ ele} = \frac{Q_{ann\ ele}}{0.38 \times 29.3\ kWh/therm} = 4.9\ therms/(m^2\ year) \quad (37)$$

$$NG_{saved\ th} = \frac{Q_{ann\ th}}{29.3\ kWh/therm} = 2.9\ therms/(m^2\ year) \quad (38)$$

714 4.7.3 Monetary savings from the LCPV/T system

715 Renewable energy systems once installed does not require much maintenance because of which they
716 immediately start generating revenue. In this section monetary benefits of the installation of the LCPV/T
717 system are calculated. By installing the LCPV/T system, annual energy savings of 187 kWh_e/yr and 287
718 kWh_{th}/yr is observed as calculated in the previous section. Assuming the unit price of electrical energy
719 in Chennai to be INR. 5, the total yearly cost savings is observed to be INR. 937 from the electrical and
720 INR. 546 from the thermal output. The thermal output is calculated by first converting the thermal output
721 to equivalent electrical output by a conversion factor of 0.38 [41].

722 4.7.4 Reduction in carbon emission from the LCPV/T system.

723 Electricity generated in any thermal power plant is at the expense of carbon emission. These carbon
724 emissions pollute the environment and result in global warming. To mitigate that, renewable sources of
725 energy are explored. Integration of the LCPV/T system to the desiccant-based air cooler is also carried
726 out keeping in mind the carbon emission from the air conditioners. For the present case, the electrical
727 and thermal energy generated by the LCPV/T system is converted to equivalent carbon emission from
728 the natural gas as calculated in section 5.6.2. For natural gas, the carbon dioxide emission factor is 5.3
729 kg of CO₂/therm [41]. Using the emission factor, the carbon dioxide emission mitigated by the LCPV/T
730 system is calculated by equation (39-40).

$$CO_2\ emission = NG_{saved\ th} \times 5.3 = 15.29\ kg/(m^2\ year) \quad (39)$$

$$CO_2\ emission = NG_{saved\ el} \times 5.3 = 26.25\ kg/(m^2\ year) \quad (40)$$

732 5 Conclusions

733 In this work, a coupled optical, electrical, and thermal model has been developed for predicting the
734 performance of the system. The key conclusions that can be drawn from the present work can be
735 summarized below.

- 736 • Flux obtained in the case of CPC was observed to be non-uniform. The non-uniform flux has
737 been mitigated by introducing an optimized linear homogenizer measuring 400 mm length to the
738 CPC.. The spatial non-uniformity factor and average concentration ratio were observed to be
739 0.28 and 1.66, respectively.
- 740 • A coupled optical electrical and thermal model was developed to predict the system
741 performance. Comparison between simulated and measured thermal performance showed
742 close match with relative error under 6%.
- 743 • Optical simulation results show that CPC has higher optical efficiency compared to the ECPC. It
744 is expected that CPC will perform better in terms of electrical and thermal performance. However,
745 the electrical simulation results are completely unexpected. Results show improved electrical
746 performance for the case of ECPC instead of CPC between 0-10° angle of incidence primarily
747 due to the uniform distribution of flux in the case of ECPC. Further analysis of the results shows
748 that at a normal angle of incidence, the electrical performance of the ECPC was 12% improved
749 compared to CPC. However, the thermal simulation results followed the expected trend where
750 the thermal performance of CPC is 1-2% better than the ECPC due to higher optical efficiency.
- 751 • Results of thermal simulation for the stagnation condition showed that the intracell thermal
752 gradient is highest for the case of CPC based LCPV/T system. This thermal gradient further
753 increases with an increase in the angle of incidence. Near the acceptance angle, almost all the
754 rays concentrate on one column of the solar cells resulting in the formation of the thermal hot
755 spot and thermal-induced fatigue which results in relatively faster degradation of the solar cells.
- 756 • Simulation results for the coupling of the LCPV/T system to the desiccant-based air cooler
757 showed an improvement in COP by 50%.
- 758 • The LCPV/T system installation results in the mitigation of 15 kg/year and 26 kg/year of carbon
759 emission from the thermal and electrical output, respectively. Overall cost savings by the system
760 is observed to be INR. 936/year and INR. 546/year from the electrical and thermal output,
761 respectively.
- 762 •

763 In the future, it is proposed that side by side testing of the LCPV/T system integrated with CPC and
764 ECPC will be carried out. Further, to increase the working hours of the ECPC based LCPV/T system, a
765 tracking mechanism will also be explored.

766 6 Acknowledgement

767 The authors acknowledge the funding support of DST through sanction letter no DST/TM/SERI/278(G).
768 The financial support (in the form of Senior Research Fellow) received from [CSIR HRDG](#) by the first author
769 is also acknowledged.

770

771 7 References

- 772 [1] C. Gnanaseelan, M. Mujumdar, A. Kulkarni, S. Chakraborty, and E. Sciences, *Assessment of*
773 *Climate Change over the Indian Region*. 2020.
- 774 [2] M. A. Green, K. Emery, Y. Hishikawa, and W. Warta, "Solar cell efficiency tables (version 37),"
775 *Prog. Photovoltaics Res. Appl.*, vol. 19, no. 1, pp. 84–92, 2011.

- 776 [3] A. Heidari, R. Roshandel, and V. Vakiloroaya, "An innovative solar assisted desiccant-based
777 evaporative cooling system for co-production of water and cooling in hot and humid climates,"
778 *Energy Convers. Manag.*, vol. 185, no. August 2018, pp. 396–409, 2019.
- 779 [4] H. A. Zondag, "Flat-plate PV-Thermal collectors and systems: A review," *Renew. Sustain.*
780 *Energy Rev.*, vol. 12, no. 4, pp. 891–959, 2008.
- 781 [5] M. Herrando, C. N. Markides, and K. Hellgardt, "A UK-based assessment of hybrid PV and
782 solar-thermal systems for domestic heating and power: System performance," *Appl. Energy*,
783 vol. 122, pp. 288–309, 2014.
- 784 [6] T. Ma, M. Li, and A. Kazemian, "Photovoltaic thermal module and solar thermal collector
785 connected in series to produce electricity and high grade heat simulataneously," *Appl. Energy*,
786 vol. 261, no. 1 March 2020, p. 114380, 2020.
- 787 [7] H. Baig, H. Kanda, A. M. Asiri, M. K. Nazeeruddin, and T. Mallick, "Increasing efficiency of
788 perovskite solar cells using low concentrating photovoltaic systems," *Sustain. Energy Fuels*, vol.
789 4, no. 2, pp. 528–537, 2020.
- 790 [8] M. Tian, Y. Su, H. Zheng, G. Pei, G. Li, and S. Riffat, "A review on the recent research progress
791 in the compound parabolic concentrator (CPC) for solar energy applications," *Renew. Sustain.*
792 *Energy Rev.*, vol. 82, no. September 2017, pp. 1272–1296, 2018.
- 793 [9] A. Al-Alili, Y. Hwang, R. Radermacher, and I. Kubo, "A high efficiency solar air conditioner using
794 concentrating photovoltaic/thermal collectors," *Appl. Energy*, vol. 93, pp. 138–147, 2012.
- 795 [10] Y. Liu *et al.*, "Performance evaluation of a hybrid solar powered rotary desiccant wheel air
796 conditioning system for low latitude isolated islands," *Energy Build.*, vol. 224, p. 110208, 2020.
- 797 [11] S. Tian, X. Su, X. Shao, and L. Wang, "Optimization and evaluation of a solar energy, heat
798 pump and desiccant wheel hybrid system in a nearly zero energy building," *Build. Simul.*, vol.
799 13, no. 6, pp. 1291–1303, 2020.
- 800 [12] N. Wang *et al.*, "Performance assessment of PCM-based solar energy assisted desiccant air
801 conditioning system combined with a humidification-dehumidification de5salination unit,"
802 *Desalination*, vol. 496, no. August, p. 114705, 2020.
- 803 [13] J. Paul, E. Katramiz, K. Ghali, D. Ouahrani, and N. Ghaddar, "Comparative analysis of
804 sustainable desiccant – Evaporative based ventilation systems for a typical Qatari poultry
805 house," *Energy Convers. Manag.*, vol. 245, p. 114556, 2021.
- 806 [14] T. Hu, Y. Shen, T. Hocksun, and G. Pei, "Absorption chiller waste heat utilization to the
807 desiccant dehumidifier system for enhanced cooling e Energy and exergy analysis," *Energy*,
808 vol. 239, p. 121847, 2022.
- 809 [15] X. Zhou, "Thermal and energy performance of a solar-driven desiccant cooling system using an
810 internally cooled desiccant wheel in various climate conditions," *Appl. Therm. Eng.*, vol. 185, no.
811 April 2020, p. 116077, 2021.
- 812 [16] M. Jagirdar, P. Seng, and J. T. Padding, "Performance of an internally cooled and heated
813 desiccant-coated heat and mass exchanger : Effectiveness criteria and design methodology,"
814 *Appl. Therm. Eng.*, vol. 188, no. January, p. 116593, 2021.
- 815 [17] C. Roselli, M. Sasso, and F. Tariello, "Assessment of a solar PV-driven desiccant-based air
816 handling unit with different tracking systems," *Sustain. Energy Technol. Assessments*, vol. 34,
817 no. March, pp. 146–156, 2019.
- 818 [18] X. Ju, M. M. Abd El-Samie, C. Xu, H. Yu, X. Pan, and Y. Yang, "A fully coupled numerical
819 simulation of a hybrid concentrated photovoltaic/thermal system that employs a therminol VP-1

- 820 based nanofluid as a spectral beam filter,” *Appl. Energy*, vol. 264, no. February, p. 114701,
821 2020.
- 822 [19] R. V. Parupudi, H. Singh, and M. Kolokotroni, “Low Concentrating Photovoltaics (LCPV) for
823 buildings and their performance analyses,” *Appl. Energy*, vol. 279, no. August, p. 115839, 2020.
- 824 [20] M. Abdelhamid *et al.*, “Novel double-stage high-concentrated solar hybrid photovoltaic/thermal
825 (PV/T) collector with nonimaging optics and GaAs solar cells reflector,” *Appl. Energy*, vol. 182,
826 pp. 68–79, 2016.
- 827 [21] A. Moaleman, A. Kasaeian, M. Aramesh, O. Mahian, L. Sahota, and G. Nath Tiwari, “Simulation
828 of the performance of a solar concentrating photovoltaic-thermal collector, applied in a
829 combined cooling heating and power generation system,” *Energy Convers. Manag.*, vol. 160,
830 no. July 2017, pp. 191–208, 2018.
- 831 [22] H. Baig *et al.*, “Conceptual design and performance evaluation of a hybrid concentrating
832 photovoltaic system in preparation for energy,” *Energy*, vol. 147, no. February, pp. 547–560,
833 2018.
- 834 [23] N. Sellami and T. K. Mallick, “Optical efficiency study of PV Crossed Compound Parabolic
835 Concentrator,” *Appl. Energy*, vol. 102, no. February, pp. 868–876, 2013.
- 836 [24] J. Chaves, *Introduction to nonimaging optics*, 1st ed. 2008.
- 837 [25] H. Baig, N. Sellami, and T. K. Mallick, “Optical Analysis of a Cpc Based Cpv / T System for
838 Application in,” in *28th EU PVSEC 2013:Paris*, 2013, no. September, pp. 653–657.
- 839 [26] H. Chen *et al.*, “Experimental Investigation of a Novel LCPV/T System with Micro -channel Heat
840 Pipe Array,” *Renew. energy*, vol. Volume 115, no. January 2018, pp. 773–782, 2017.
- 841 [27] G. Li, G. Pei, J. Ji, and Y. Su, “Outdoor overall performance of a novel air-gap-lens-walled
842 compound parabolic concentrator (ALCPC) incorporated with photovoltaic / thermal system,”
843 *Appl. Energy*, vol. 144, pp. 214–223, 2015.
- 844 [28] H. Hadavinia and H. Singh, “Modelling and experimental analysis of low concentrating solar
845 panels for use in building integrated and applied photovoltaic (BIPV/BAPV) systems,” *Renew.*
846 *Energy*, vol. 139, no. August, pp. 815–829, 2019.
- 847 [29] A. H. Jaaz, K. Sopian, and T. S. Gaaz, “Study of the electrical and thermal performances of
848 photovoltaic thermal Collector-Compound parabolic concentrated,” *Results Phys.*, vol. 9, no.
849 March, pp. 500–510, 2018.
- 850 [30] H. Baig, N. Sellami, D. Chemisana, J. Rosell, and T. K. Mallick, “Performance analysis of a
851 dielectric based 3D building integrated concentrating photovoltaic system,” *Sol. Energy*, vol.
852 103, pp. 525–540, 2014.
- 853 [31] X. Chen and X. Yang, “Solar collector with asymmetric compound parabolic concentrator for
854 winter energy harvesting and summer overheating reduction: Concept and prototype device,”
855 *Renew. Energy*, vol. 173, pp. 92–104, 2021.
- 856 [32] H. Baig, R. Jani, B. K. Markam, S. Maiti, and T. K. Mallick, “Modelling and experimental analysis
857 of a seasonally tracked V-trough PV / T system in India,” vol. 170, no. December 2017, pp.
858 618–632, 2018.
- 859 [33] S. Sharma, A. Tahir, K. S. Reddy, and T. K. Mallick, “Solar Energy Materials & Solar Cells
860 Performance enhancement of a Building-Integrated Concentrating Photovoltaic system using
861 phase change material,” *Sol. Energy Mater. Sol. Cells*, vol. 149, pp. 29–39, 2016.
- 862 [34] Z. Heng, L. Kai, C. Haiping, G. Dan, and G. Xinxin, “Thermal and electrical performance of low-

- 863 concentrating PV/T and flat-plate PV/T systems: A comparative study," *Energy*, vol. 177, no. 15
864 June 2019, pp. 66–76, 2019.
- 865 [35] M. S. Yousef, A. K. Abdel Rahman, and S. Ookawara, "Performance investigation of low –
866 Concentration photovoltaic systems under hot and arid conditions: Experimental and numerical
867 results," *Energy Convers. Manag.*, vol. 128, no. March 2017, pp. 82–94, 2016.
- 868 [36] B. Widyolar *et al.*, "Experimental performance of an ultra-low-cost solar photovoltaic-thermal
869 (PVT) collector using aluminum minichannels and nonimaging optics," *Appl. Energy*, vol. 268,
870 no. October 2019, p. 114894, 2020.
- 871 [37] G. Zhang, J. Wei, Z. Wang, H. Xie, Y. Xi, and M. Khalid, "Investigation into effects of non-
872 uniform irradiance and photovoltaic temperature on performances of photovoltaic/thermal
873 systems coupled with truncated compound parabolic concentrators," *Appl. Energy*, vol. 250, no.
874 April, pp. 245–256, 2019.
- 875 [38] D. Freier Raine, R. Ramirez-Iniguez, T. Jafry, F. Muhammad-Sukki, and C. Gamio, "Design
876 method of a compact static nonimaging concentrator for portable photovoltaics using
877 parameterisation and numerical optimisation," *Appl. Energy*, vol. 266, no. March, 2020.
- 878 [39] Q. Xuan *et al.*, "Performance evaluation for the dielectric asymmetric compound parabolic
879 concentrator with almost unity angular acceptance efficiency," *Energy*, vol. 233, p. 121065,
880 2021.
- 881 [40] Y. Li, F. Jiao, F. Chen, and Z. Zhang, "Design optimization and optical performance analysis on
882 multi-sectioned compound parabolic concentrator with plane absorber," *Renew. Energy*, vol.
883 168, pp. 913–926, 2021.
- 884 [41] H. Machrafi, "Enhancement of a photovoltaic cell performance by a coupled cooled
885 nanocomposite thermoelectric hybrid system, using extended thermodynamics," *Curr. Appl.
886 Phys.*, vol. 17, no. 6, pp. 890–911, 2017.
- 887 [42] Chandan, S. Dey, P. Sujana Kumar, K. S. Reddy, and B. Pesala, "Optical and electrical
888 performance investigation of truncated 3X non-imaging low concentrating photovoltaic-thermal
889 systems," *Energy Convers. Manag.*, vol. 220, no. May, p. 113056, 2020.
- 890 [43] G. Angrisani, F. Minichiello, and M. Sasso, "Experimental analysis of an unconventional
891 desiccant-based air-conditioning system: The influence of cooling air flow and chiller on the
892 energy and environmental performance," *Int. J. Low-Carbon Technol.*, vol. 10, no. 4, pp. 321–
893 331, 2015.
- 894 [44] D. B. Jani, M. Mishra, and P. K. Sahoo, "Experimental investigation on solid desiccant-vapor
895 compression hybrid air-conditioning system in hot and humid weather," *Appl. Therm. Eng.*, vol.
896 104, pp. 556–564, 2016.
- 897 [45] H. Baig, N. Sarmah, K. C. Heasman, and T. K. Mallick, "Numerical modelling and experimental
898 validation of a low concentrating photovoltaic system," *Sol. Energy Mater. Sol. Cells*, vol. 113,
899 pp. 201–219, 2013.
- 900 [46] M. M. Khan, S. M. Iqbal, N. T. Ravi, and B. Pesala, "Design and development of an optical
901 system for obtaining fixed orientation of concentrated sunlight for indoor applications," *Solar
902 Energy*, vol. 204, pp. 515–529, 2020.
- 903 [47] A. Parthiban, K. S. Reddy, B. Pesala, and T. K. Mallick, "Effects of operational and
904 environmental parameters on the performance of a solar photovoltaic-thermal collector," *Energy
905 Convers. Manag.*, vol. 205, no. December 2019, p. 112428, 2020.
- 906 [48] S. P. Venkateshan, *Mechanical Measurement*, 2nd ed. John Wiley & Sons Ltd, 2015.

907

908

909